
Modelling and Control of a Three Phase Inverter

Bachelor's Thesis
IEL6-1-F24

Aalborg University
AAU Energy

Copyright © Aalborg University 2024

L^AT_EX used for formatting. MATLAB R203a Update 1 (9.14.0.2239454) and Simulink R203a (10.7) used for plots and simulations. Inkscape 1.1 (c68e22c387, 2021-05-23) used for plot editing.



AALBORG UNIVERSITY
STUDENT REPORT

Energy Department
Aalborg University
<http://www.aau.dk>

Title:

Modelling and Control of
a Three Phase Inverter

Theme:

Modelling and Control of
Industrial Electronic Applications

Project Period:

Spring Semester 2024

Project Group:

IEL6-1-F24

Participant(s):

Boris Fabula
Nils Albin Emil Nolemo
Miguel Ángel García Otalora

Supervisor(s):

Amin Hajizadeh

Copies: 1

Page Numbers: 60

Date of Completion:

July 24, 2024

Abstract:

The concept of power barges is not novel, with the first fossil fuel floating power plant appearing in the 1940s. As the world transitions towards renewable sources of electricity, their inherent weather dependency calls for solutions that can store the energy during overproduction and deliver it on demand. Research and development of green power barges are gaining traction and projects like BlueBARGE call on international cooperation to seek to develop new solutions for power bunkering using marine vessels.

The report investigates modelling and control methods for three phase inverter technologies that could be applicable in battery energy storage systems on power barges. The requirements of the inverter under different use cases are considered, with the focus placed on grid connected operation.

Objectives for the project are inspired by the regulations imposed by the Danish grid operator. PI and state-space control methods together with L and LCL filtering of the inverter output are compared to assess the advantages of different approaches.

The content of this report is freely available, but publication (with reference) may only be pursued due to agreement with the authors.



AALBORG UNIVERSITY
STUDENT REPORT

Institut for Energi
Aalborg Universitet
<http://www.aau.dk>

Titel:

Modellering og Regulering af
en Trefaset Inverter

Tema:

Modellering og Styring af
Industrielle Elektroniske Applikationer

Projektperiode:

Forårssemester 2024

Projektgruppe:

IEL6-1-F24

Deltagere:

Boris Fabula
Nils Albin Emil Nolemo
Miguel Ángel García Otalora

Vejleder:

Amin Hajizadeh

Oplagstal: 1

Sidetæl: 60

Afleveringsdato:

July 24, 2024

Abstract:

Konceptet med kraftværkspramme er ikke noget nyt, da de første flydende kraftværker, der kørte på fossile brændstoffer, dukkede op i 40'erne. Når verden går over til vedvarende energi, er der brug for lagringsteknologier for at kompensere for dens vejrafhængighed. Forskning og udvikling af miljøvenlige kraftværkspramme bliver mere populært, og projekter som BlueBARGE kræver internationalt samarbejde for at udvikle løsninger inden for marine energitransmission.

Denne rapport undersøger modellerings- og regulerings-metoder for inverterteknologier, som i fremtiden kan bruges i batterilagringsløsninger på disse pramme. Kravene til konverteren under forskellige scenarier tages i betragtning med fokus på nettilsluttet drift.

Projektets formål er inspireret af de regler, der er pålagt af den danske netoperatør. PI og state-space reguleringsmetoder sammen med L- og LCL-filtrering af inverterns strømforsyning sammenlignes for at evaluere fordele ved forskellige metoder.

The content of this report is freely available, but publication (with reference) may only be pursued due to agreement with the authors.

Contents

Preface	vii
Acronyms	viii
Symbols	ix
1 Introduction	1
2 Problem Analysis	2
2.0.1 AC Side Electrical Requirements and Regulations	2
2.0.2 DC Side Parameters	4
2.0.3 Commercially Available Power Converters	5
2.0.4 Project Scope Delimitation	5
3 Problem Solution	7
3.1 System Overview	7
3.2 DC Bus	8
3.3 Grid	8
3.4 Inverter	8
3.5 Modulator	8
3.6 Filter Design	9
3.6.1 L Filter Model	10
3.6.2 LCL Filter Model	12

3.7	Sizing of Filter Components	15
3.8	Phase-Locked Loop	18
3.8.1	Primary Analysis	18
3.8.2	Control	19
3.9	Control	20
3.9.1	Power Control	20
3.9.2	Transfer Function Analysis	21
3.9.3	PI Current Control	23
3.9.4	State-Space Current Control	25
4	Simulation	31
4.1	Reference Tracking	31
4.1.1	L Filter	32
4.1.2	LCL Filter	33
4.2	Harmonic Distortion	37
4.3	Grid Stiffness Test	38
4.4	Line Fault Test	41
4.4.1	Original PI Controller	42
4.4.2	Adjusted PI Controller	43
5	Discussion and Conclusion	46
5.1	Discussion	46
5.2	Conclusion	47
	Bibliography	48
A	Matlab Modelling Code	53
A.1	Matlab Code for PI L/LCL Control Derivation	53
A.2	Matlab Code for L State Space Control Derivation	54

A.3	Matlab Code f or LCL State Space Control Derivation	55
A.4	Matlab Code for Calculating L_{grid} and R_{grid} for Weak Grids	56
B	Simulink Figures	57

Preface

This report was done as the bachelor project of the sixth semester group IEL6-1-F24 of the Applied Industrial Electronics program at Aalborg University in Esbjerg. The project was completed as part of fulfilling the curriculum for the project course **Modelling and Control of Industrial Electronic Applications**.

Aalborg University, July 24, 2024



Boris Fabula
<bfabul21@student.aau.dk>



Nils Albin Emil Nolemo
<nnolem21@student.aau.dk>



Miguel Angel Garcia Otalora
<maga21@student.aau.dk>

Nomenclature

Acronyms

Acronym	Definition
BESS	Battery Energy Storage Systems
CSI	Current Source Inverter
DK1	The West Denmark Grid Region
IGBT	Insulated-Gate Bipolar Transistor
KCL	Kirchhoff's Current Law
KVL	Kirchhoff's Voltage Law
L	Inductor (inverter filter)
LCL	Inductor Capacitor Inductor (inverter filter)
LQR	Linear Quadratic Regulator
PID	Proportional–Integral–Derivative
PLL	Phase-Locked Loop
PWM	Pulse-Width Modulation
SS	State-space
THD	Total Harmonic Distortion
VSI	Voltage Source Inverter

Symbols

Symbol	Unit	Definition
V_{DC}	V	DC voltage
E_N, E_{ph}	V	Converter nominal line-to-line and phase RMS voltages
S_N	W	Converter apparent output power
$S_1 - S_6$		Inverter switches
a, b, c		Phases
A, B, C, D		Matrices of the state-space representation
I		Identity matrix
X, U, Y		State, input, and output vectors in state-space
\dot{X}		Derivative of the state vector in state-space
dq		Direct-quadrature frame
θ	rad	Initial phase angle of the phases in ABC
ω	rad/s	Angular frequency of the rotating reference frame in DQ
v_i	V	Inverter-side voltage In <i>abc</i> -frame: v_{ia}, v_{ib}, v_{ic} In <i>dq</i> -frame: v_{id}, v_{iq}
v_g	V	Grid-side voltage In <i>abc</i> -frame: v_{ga}, v_{gb}, v_{gc} In <i>dq</i> -frame: v_{gd}, v_{gq}
i_i	A	Inverter-side current In <i>abc</i> -frame: i_{ia}, i_{ib}, i_{ic} In <i>dq</i> -frame: i_{id}, i_{iq}
i_g	A	Grid-side current In <i>abc</i> -frame: i_{ga}, i_{gb}, i_{gc} In <i>dq</i> -frame: i_{gd}, i_{gq}
L, R	H, Ω	L-filter inductance and parasitic resistance
L_i, R_i	H, Ω	LCL-filter inverter-side inductance and parasitic resistance
L_g, R_g	H, Ω	LCL-filter grid-side inductance and parasitic resistance
L_{grid}, R_{grid}	H, Ω	Grid inductance and resistance
Z_{grid}	Ω	Grid impedance
C_f	F	LCL-filter capacitance
v_{L_i}, v_{L_g}	V	Voltage drops across each LCL-filter inductor
v_{C_f}	V	Voltage drop across the LCL-filter capacitor In <i>abc</i> -frame: $v_{C_fa}, v_{C_fb}, v_{C_fc}$ In <i>dq</i> -frame: v_{C_fd}, v_{C_fq}
i_{C_f}	A	Current across the LCL-filter capacitor In <i>abc</i> -frame: $i_{C_fa}, i_{C_fb}, i_{C_fc}$ In <i>dq</i> -frame: i_{C_fd}, i_{C_fq}
\dot{v}, \dot{i}	V/s, A/s	Time derivatives of voltage and current
s		Laplace complex variable
$\omega_0, \omega_{sw}, \omega_r$	rad/s	Grid, switching, and resonant angular frequencies
f_0, f_{sw}, f_r	Hz	Grid, switching, and resonant frequencies
K_p, K_i		Proportional and integral gains
ω_n	rad	Natural frequency
ζ		Damping ratio
τ		Time constant
α	rad	Phase angle shift
P	W	Active power
Q	VA _r	Reactive power
S_{SC}	VA	Short-circuit power
SCR		Short-circuit ratio

Chapter 1

Introduction

Power barges are a useful asset in the current energy landscape. Due to their mobility, they can cover a demand where it is generated for a specific time frame and then be relocated to cover another demand. Floating power plants have evolved since their inception during World War II[1], and barges that can be run off various fuels, including liquefied natural gas, petroleum, diesel, heavy fuel oil, and nuclear fuel have been developed[2].

With the expansion of renewable energies and their presence in the energy mix comes the need to store surplus production and release it when needed. Countries like Denmark and Uruguay frequently produce more clean energy than they can use[3, 4], therefore the use of green storage solutions, such as hydrogen or batteries, takes an important role.

In this context of renewables, the use of battery power barges is being researched and developed. The EU funded project BlueBARGE involves partners from ten European countries and aims to develop a comprehensive solution for power bunkering moored and anchored ships[5]. Given that an estimated 60 % of marine emissions are produced at berthing and while entering or leaving ports, this could be an important use case[6].

Additionally, battery power barges could be used to connect to coastal regions to alleviate grid stress during high-demand periods and to provide grid stabilisation[7]. Power barges are already being used in grid applications, with the nuclear barge Akademik Lomonosov being used since 2019 to provide remote regions with power and heat[8].

With a growing interest in combining modern renewable technology and barge applications, this report aims to investigate some of the potential restrictions and technical challenges these could face, with a focus on the DC-AC energy conversion technology required to interface between battery and load.

Chapter 2

Problem Analysis

Since a power barge based on a battery energy storage system (BESS) is explored, the system requires all the components of a regular BESS, namely a battery array, an inverter, and the equipment facilitating connection to grid which includes a filter[9]. In this chapter, a number of legal regulations and electrical parameters of a BESS are discussed based on researched literature.

The purpose of this problem analysis is to narrow down relevant legal requirements that would pertain to the conversion technology required for these barges, and investigate relevant inverter topologies that could be used to fulfil the aforementioned requirements.

2.0.1 AC Side Electrical Requirements and Regulations

In order to implement a BESS as a supply of electricity, it is crucial that it follows standards and regulations related to voltage, current, and frequency, among others. These requirements can differ based on the use case, and so this section provides a review of the requirements of two possible scenarios where a power barge could be used: shore power and grid stabilisation.

If the power barge is to provide power to other marine vessels, its electric system should be able to deliver power according to the most commonly used specifications of hybrid ships. Vessels that are equipped to utilise shore power need to receive the same voltage as used by own internal systems. This voltage is 400 V or 690 V for small to medium sized ships. Larger cargo ships or passenger cruise ships use 3.3 to 11 kV. Moreover, there is no one standard AC frequency for ships and thus the shore power system may need to be able to operate at both 50 and 60 Hz[10].

Connection of a power source to a grid is strictly regulated. Below is an outline of some of

the main requirements for grid connection in Denmark's DK1 grid system as described in technical standards set by Energinet, the Danish grid operator[11]. It should however be noted that this is not an exhaustive list of all requirements.

Categories of storage facilities are defined per their output power rating, and affect the technical requirements. The categories are given in table 2.1.

Table 2.1: Power ratings of different categories of grid-connected storage systems as per Danish standards.

Category	Span [kW]
A	0 - 125
B	125 - 2 999
C	3 000 - 24 999
D	$\geq 25\,000$

Given that battery power barges are in the prototyping phase, the categories A and B, the less powerful side of the specified ratings, will be considered further as it is considered more relevant at this stage.

Phase requirements are such that any system operating above 3.68 kW/16 A is required to transmit power over multiple phases, and if it is over 11 kW it must be three-phase.

Voltage levels are similarly categorised, defining low, medium and high voltage distribution in the Danish grid as shown in table 2.2.

Table 2.2: Upper and lower voltage levels that define the categories of voltage distribution levels in the Danish grid.

Category	Span [kV]
Low Voltage	0.4 - 0.69
Medium Voltage	10 - 33
High Voltage	50 - 60

DC injection to the grid must be limited to 0.5 % of total current.

System recovery time of a system of category B, C and D should be at most 5 seconds after a voltage dip.

Harmonics are an important measure to take into consideration. Standards are set both for total distortion as well as for specific harmonics. The standards are defined in relation to a percentage of the current and the short circuit ratio of the grid.

Table 2.3: Requirements for THD defined per rated voltage and SCR.

	SCR	THD [%]
$V_{rated} \leq 1 \text{ kV}$	< 33	4.4
	≥ 33	4.7
	≥ 66	6.1
	≥ 120	8.4
	≥ 250	13.8
	≥ 350	18.0
$V_{rated} > 1 \text{ kV}$	-	4.4

Table 2.4: Specific requirements for harmonic orders of the primary frequency.

	SCR	Odd harmonic order h							Even harmonic order h					
		3	5	7	9	11	13	15	2	4	6	8	10	12
$U \leq 1 \text{ kV}$	< 33	3.4	3.8	2.5	0.5	1.2	0.7	0.35	0.5	0.5	1.0	0.8	0.6	0.5
	≥ 33	3.5	4.1	2.7	0.5	1.3	0.7	0.37	0.5	0.5	1.0	0.8	0.6	0.5
	≥ 66	3.9	5.2	3.4	0.6	1.8	1.0	0.43	0.5	0.5	1.0	0.8	0.6	0.5
	≥ 120	4.6	7.1	4.6	0.8	2.5	1.5	0.5	0.5	0.5	1.0	0.8	0.6	0.5
	≥ 250	6.3	11.6	7.3	1.3	4.4	2.7	0.8	0.5	0.5	1.0	0.8	0.6	0.5
	≥ 350	7.5	15.0	9.5	1.6	5.7	3.7	1.0	0.5	0.5	1.0	0.8	0.6	0.5
$U > 1 \text{ kV}$	-	3.4	3.8	2.5	0.5	1.2	0.7	0.35	0.5	0.5	1.0	0.8	0.6	0.5

2.0.2 DC Side Parameters

Electrical parameters of the power barge depend on the designated use case, as some applications may require different power outputs, response times, and capacities. The battery capacity has a direct impact on the size of the barge, its manoeuvrability in ports and the ship building cost.

Decisions regarding the battery capacity and DC bus voltage of the BESS system considered in this project are based on existing commercial products. Two examples of such products are represented by CPS-i by Dynapower[12] and Intensium Shift by Saft[13]. These systems use a DC bus voltage of up to 1 500 V and offer a capacity of 3 MWh per standard 20 ft shipping container. This parameter can be used as an estimate for specifying the size of a power barge, although it should be noted that the considered systems are not designed for marine conditions. Nevertheless, the model in this project will be designed for a system with 1 500 V at the DC bus.

2.0.3 Commercially Available Power Converters

Multiple vendors have products that are implemented for cold ironing applications[14, 15] with battery energy storage systems. Power converters are key to achieve the desired output while complying with regulations and requirements. These converters need to be coupled with the adequate transformer and filter configuration. Table 2.5 shows three lines of products by different manufacturers.

Table 2.5: Characteristics of commercial power converters from Danfoss[16, 17], ABB[18], and Siemens[19].

Vendor	Product	Configuration	Operation	Control	THD	Standards
Danfoss	Vacon NXP Grid	3-phase IGBT Bridge	Active Front End Island μ Grid	Droop Isochron	<5 % THDi	IEC62116 EN50549 (1,2) ENTSO-e (031)
ABB	PCS100	3-phase 2-level Full-bridge IGBT	VSI CSI	Droop Isochron Power setpoint	<8 % THDv	IEC 62103 IEC61000 (6-2) IEEE 519 IEEE10 (2000)
Siemens	Sinamics S120 AI	3-phase Active infeed IGBT Bridge	Power grid Island μ Grid	Transformer Droop Dynamic	IEEE519 compliant	EN61800 (5-1 & 3) UL508C IEEE 519

It is worth noting that, being patented products, the complete diagrams are not available, nevertheless they can be used as reference for topology, control techniques, THD, and certifications.

2.0.4 Project Scope Delimitation

Taking into consideration the variety of applications that power barges could be used for, such as grid support or powering ships, this means the system could need to be able to operate at many different voltage levels and with several different control methods depending on the application. However, for this project the focus will be on low voltage grid-tied applications. This will entail the inverter design to be centred around a 400 V_{l-l} grid and a maximum power rating of 500 kW, which is designated as a conservative, proof-of-concept scale power output. While designing a fully regulation-compliant inverter is not

feasible in the context of a semester project, the report attempts to conform to some of the legal requirements specified in section 2.0.1. The focus will be on lowering the harmonic distortions in the output current, as well as conforming to DC injection requirements. This will be conducted by testing two control approaches, PID and state-space controllers.

Regarding the topology of the grid-tied inverter that will be used in the project, there are several considerations to make such as efficiency, complexity and cost. Cascaded H-bridge and modular multilevel converters have the highest efficiency of up to $\approx 98\%$ over a wide range of switching frequencies. They do however have a tendency to present low-order harmonics that may affect the battery life and compromise safety[20]. This could pose an issue for the harmonic requirements. They can also present additional challenges in terms of modelling and control due to their more complex topologies.

Cascaded and Modular inverters aside, most ubiquitous power converters are 3-level and 2-level converters, which are widely used in the industry. The 3-level converter is more efficient at lower switching frequencies by approximately 1.5% [20] and its efficiency does not decrease as much when using higher switching frequencies[21]. The advantages of the 2-level converter are lower component count and lower cost, which combined with its reduced complexity for modelling and control makes it a suitable candidate for the present project. This topology is also found in commercial converters with BESS applications[22] such as Siemens S120 presented in section 2.0.3.

Furthermore, given the examples of commercially available container sized BESS that have a V_{dc} of around $1\,500\text{ V}$, this will be used as the input voltage to the inverter.

To summarize, the project aim is to model a grid-tied, three-phase, two-level inverter with the goal of current controlled power injection to a grid. The aim will be to investigate whether this topology can be utilised to conform with THD standards per the Danish regulations. A comparison between two different control techniques will be done in order to compare which one could potentially be more suitable for these goals. Additionally, the role of the capacitor in the LCL filter is investigated, thus modelling and control is implemented for both LCL and L filters, giving an opportunity for comparison.

A table specifying the characteristics of the system is given in Table 2.6.

Table 2.6: A summary of the characteristics of the system considered in this project.

Topology	Two-level
DC Voltage	$1\,500\text{ V}$
Nominal Voltage (E_N)	$400\text{ V}_{L-I}/230\text{ V}_{rms}$
Output Power (S_N)	500 kW

Chapter 3

Problem Solution

3.1 System Overview

The following block diagram describes broadly the different subsystems the project aims to integrate into a grid-tied inverter simulation.

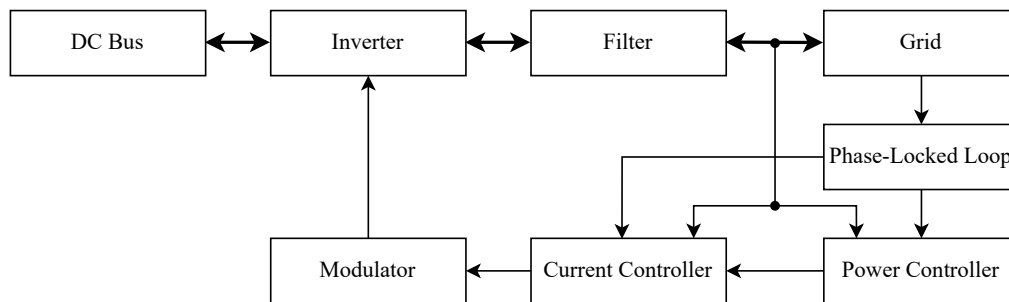


Figure 3.1: Block diagram of the proposed system. Thick lines indicate power flow, whereas thin lines symbolise measurements and control signals.

As described in Section 2.0.4, the control aspects are of primary focus, where the design and testing is varied to conclude which kind controller would be most suitable for such a system.

3.2 DC Bus

Although this project analyses an inverter in a BESS, the focus is placed on the conversion of electric power rather than storage. This means that the battery array is not modelled and the modelled inverter is instead connected to an ideal DC voltage source Simulink block that can receive and deliver power without limitations such as battery capacity, charge and discharge rates, internal resistance etc.

3.3 Grid

The grid is modelled using the Three-Phase Source block in Simulink with zero inherent inductance or resistance.

3.4 Inverter

The chosen inverter topology is a two-level three phase inverter, shown in Figure 3.2. This topology was chosen due to its relative simplicity of modelling, control and physical implementation.

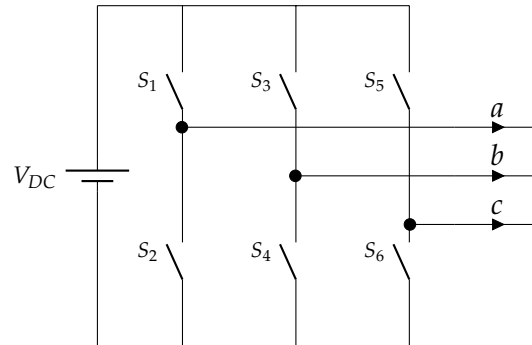


Figure 3.2: Circuit of a 2-level 3-phase inverter

3.5 Modulator

Bipolar sinusoidal PWM was chosen as the modulating technique for switching. This technique is based on comparison of a high frequency triangular waveform called carrier signal and a low frequency waveform named modulating signal. Comparison of the signals generates a switching pattern for inverter switches that are operated in complementary pairs -

if switch $S1$ is closed, switch $S2$ is open. $S1$ will be closed when the modulating waveform is greater than the carrier signal. It should be noted that this is valid for ideal switches. Real components require a so-called dead time to handle transient states.

The carrier signal has a fast-switching period T_s and amplitude $\langle -1, 1 \rangle$, while the modulating signal is typically a 50 or 60 Hz sine wave. The modulating signal shall be smaller in amplitude than the carrier signal to prevent overmodulation. Furthermore, by multiplying the abc control signals coming from the controller with $\frac{2}{V_{DC}}$ the loop gain becomes independent of V_{DC} [23]. Moreover, to limit the THD the sampling frequency needs to be an odd multiple of three and at the same time at least ten times faster than the modulation signal[24]. Increasing the switching frequency allows for smaller size of filtering components.

3.6 Filter Design

The output of an inverter will contain harmonics which can be reduced by way of filtering. This section derives the necessary models of the LCL and L filter required for control design.

In both of the examined filter models KVL and KCL circuit analysis is performed. Current and voltage equations for all three phases are rearranged as $\dot{\mathbf{X}} = \mathbf{A}\mathbf{X} + \mathbf{B}\mathbf{U}$, where \mathbf{A} is the state matrix, \mathbf{B} is the input matrix, \mathbf{X} is the state vector, and \mathbf{U} is the control input vector. Thus, choosing capacitor current and inductor voltage as the states, continuous, linear, time-invariant state-space models are obtained. Then, the transfer function of the systems is calculated by applying the transformation $\mathbf{C}(s\mathbf{I} - \mathbf{A})^{-1}\mathbf{B} + \mathbf{D}$, used to derive and test traditional PI control methods. Moreover, the state-space models are transformed from abc - to dq -frame in order to apply SS control methods. The transformation is computed using the relationship shown in Equation (3.1). The example is shown on phase currents i , however, the relationship is the same for phase voltages v , too.

$$\begin{bmatrix} i_q \\ i_d \end{bmatrix} = T_\theta \begin{bmatrix} i_a \\ i_b \\ i_c \end{bmatrix} \quad (3.1)$$

T_θ is a transformation matrix defined as:

$$T_\theta = \frac{2}{3} \begin{bmatrix} \cos(\theta) & \cos(\theta - \frac{2\pi}{3}) & \cos(\theta + \frac{2\pi}{3}) \\ \sin(\theta) & \sin(\theta - \frac{2\pi}{3}) & \sin(\theta + \frac{2\pi}{3}) \end{bmatrix}$$

Where θ is the initial phase angle of the phases in the abc -frame. Furthermore, to express

the d -component of voltage or current in the dq -frame, the product of the q -component and grid frequency ω needs to be added to the term. Conversely, the q -component is obtained by subtracting the product of the d -component and grid frequency from its term. This can be seen in the dq -frame state-space matrices in Section 3.6.1 and 3.6.2.

3.6.1 L Filter Model

An L filtered three phase inverter is modelled by connecting each phase of the inverter to the grid through an inductor, as illustrated by Figure 3.3.

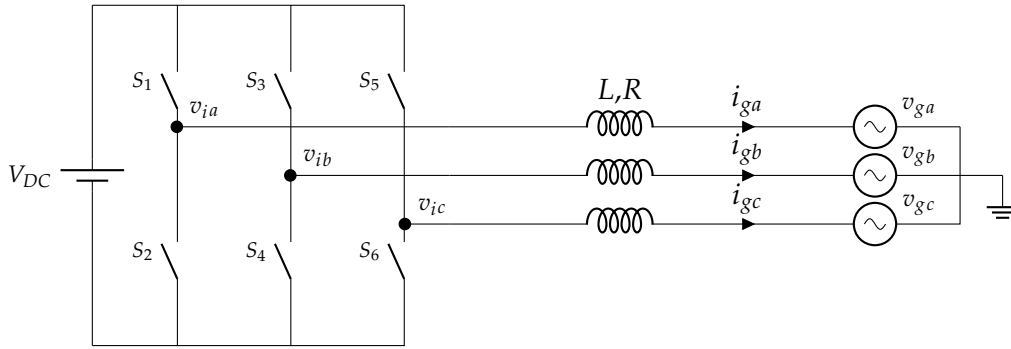
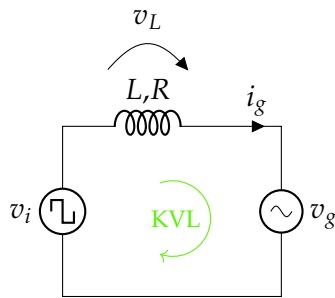


Figure 3.3: Circuit of a 2-level 3-phase inverter with an L filter.

Equation of the Circuit

The circuit is analysed using Kirchhoff's Voltage Law, represented by Figure 3.4 and Equation (3.2).



$$v_i - v_L - v_g = 0$$

$$v_L = \frac{di_g}{dt} \cdot L + R \cdot i_g$$

$$i_g = \frac{di_g}{dt} = \frac{v_i - v_g - R \cdot i_g}{L} \quad (3.2)$$

Figure 3.4: KVL of the L filter of a 2-level 3-phase inverter.

State Space

After extending Equation (3.2) to all three phases a , b , and c , the equations are rearranged into the state space form, Equations (3.3) and (3.4). The \mathbf{B} matrix is split into \mathbf{B}_1 and \mathbf{B}_2 . Similarly, the \mathbf{U} vector is split into \mathbf{U}_1 and \mathbf{U}_2 . This is motivated by the fact that the grid voltage is an uncontrolled input and thus only \mathbf{B}_1 is needed to obtain the transfer function using the transformation introduced in the beginning of Section 3.6.

$$\begin{aligned} \dot{\mathbf{X}} &= \mathbf{A} \mathbf{X} + \mathbf{B}_1 \mathbf{U}_1 + \mathbf{B}_2 \mathbf{U}_2 \\ \begin{bmatrix} \dot{i}_{ga} \\ \dot{i}_{gb} \\ \dot{i}_{gc} \end{bmatrix} &= \begin{bmatrix} R & 0 & 0 \\ -\frac{R}{L} & 0 & 0 \\ 0 & -\frac{R}{L} & 0 \\ 0 & 0 & -\frac{R}{L} \end{bmatrix} \begin{bmatrix} i_{ga} \\ i_{gb} \\ i_{gc} \end{bmatrix} + \begin{bmatrix} 1 & 0 & 0 \\ \frac{1}{L} & 0 & 0 \\ 0 & \frac{1}{L} & 0 \\ 0 & 0 & \frac{1}{L} \end{bmatrix} \begin{bmatrix} v_{ia} \\ v_{ib} \\ v_{ic} \end{bmatrix} + \begin{bmatrix} -\frac{1}{L} & 0 & 0 \\ 0 & -\frac{1}{L} & 0 \\ 0 & 0 & -\frac{1}{L} \end{bmatrix} \begin{bmatrix} v_{ga} \\ v_{gb} \\ v_{gc} \end{bmatrix} \end{aligned} \quad (3.3)$$

$$\begin{aligned} \mathbf{Y} &= \mathbf{C} \mathbf{X} + \mathbf{D} \mathbf{U} \\ \begin{bmatrix} i_{ga} \\ i_{gb} \\ i_{gc} \end{bmatrix} &= \begin{bmatrix} 1 & 0 & 0 \\ 0 & 1 & 0 \\ 0 & 0 & 1 \end{bmatrix} \begin{bmatrix} i_{ga} \\ i_{gb} \\ i_{gc} \end{bmatrix} + \begin{bmatrix} 0 \\ 0 \\ 0 \end{bmatrix} \begin{bmatrix} v_{ia} \\ v_{ib} \\ v_{ic} \\ v_{ga} \\ v_{gb} \\ v_{gc} \end{bmatrix} \end{aligned} \quad (3.4)$$

Transfer Function

The transfer function is obtained from the state-space Equations 3.3 and 3.4, presenting the result in Equation (3.5).

$$H(s) = \frac{i_g(s)}{v_i(s)} = \frac{1}{Ls + R} \quad (3.5)$$

dq -Frame

By translating the state-space model into dq -frame, Equations (3.6) and (3.7) are obtained. As before, the term including grid voltage is separated.

$$\begin{bmatrix} \dot{X} \\ \dot{Y} \end{bmatrix} = \begin{bmatrix} \mathbf{A} \\ \mathbf{C} \end{bmatrix} \mathbf{X} + \begin{bmatrix} \mathbf{B}_1 \\ \mathbf{D} \end{bmatrix} \mathbf{U}_1 + \begin{bmatrix} \mathbf{B}_2 \\ 0 \end{bmatrix} \mathbf{U}_2 \quad (3.6)$$

$$\begin{bmatrix} \mathbf{Y} \\ \mathbf{U} \end{bmatrix} = \begin{bmatrix} \mathbf{C} \\ \mathbf{D} \end{bmatrix} \mathbf{X} + \begin{bmatrix} \mathbf{D} \\ 0 \end{bmatrix} \mathbf{U} \quad (3.7)$$

3.6.2 LCL Filter Model

The LCL filter model is derived from the abc -frame representation of the circuit topology shown in Figure 3.5. Where L_i and L_g represent the inverter- and grid-side inductors, and R_i and R_g their respective parasitic resistances. C_f is the filter capacitor, whose parasitic resistance is neglected. v_i , v_{C_f} , and v_g represent the inverter-side, filter capacitor, and grid voltages respectively. i_i and i_g are the currents through each inductor and i_{C_f} is the current through the capacitor[25].

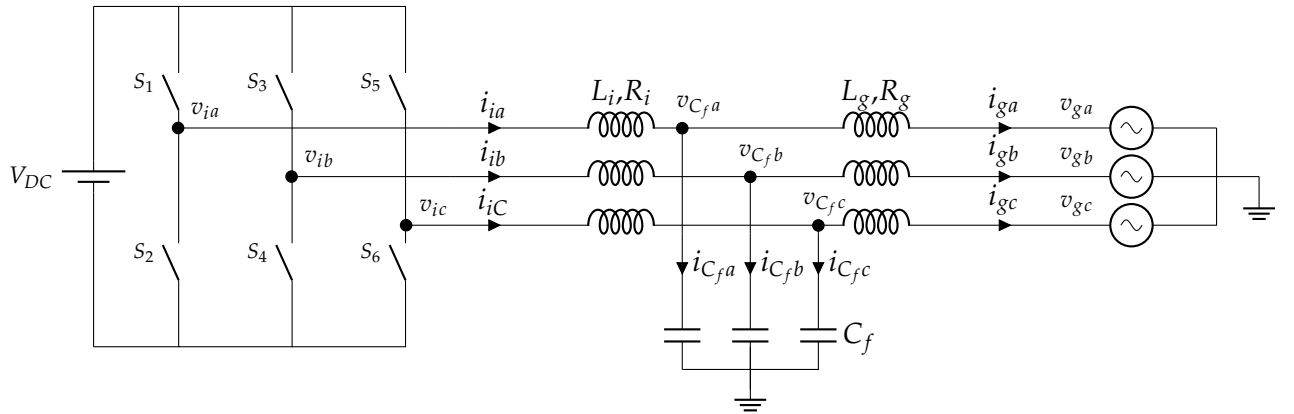


Figure 3.5: Circuit of a 2-level 3-phase inverter with a LCL filter.

Equations of the Circuit

Equations for the model are derived with Kirchhoff's Current and Voltage Laws as shown on Figures 3.6, 3.7, and 3.8 and Equations 3.8, 3.9, and 3.10.

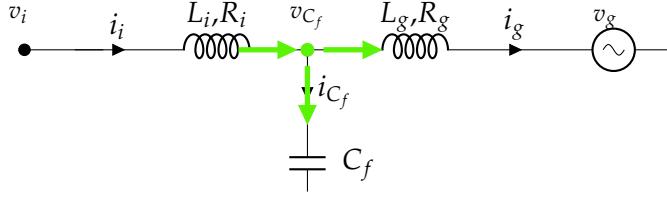
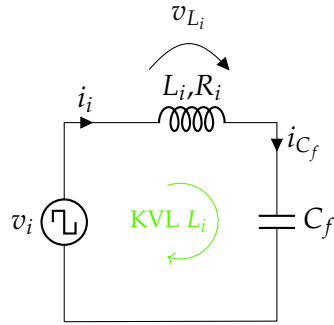


Figure 3.6: KCL of the LCL filter.

$$i_i - i_{C_f} - i_g = 0$$

$$i_{C_f} = \frac{dv_{C_f}}{dt} \cdot C_f$$

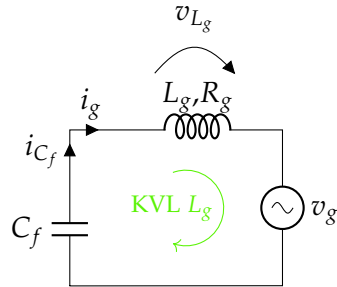
$$\dot{v}_{C_f} = \frac{dv_{C_f}}{dt} = \frac{i_i - i_g}{C_f} \quad (3.8)$$

Figure 3.7: KVL of the first inductor (L_i) of a LCL filter of a 2-level 3-phase inverter.

$$v_i - v_{L_i} - v_{C_f} = 0$$

$$v_{L_i} = \frac{di_i}{dt} \cdot L_i + R_i \cdot i_i$$

$$\dot{i}_i = \frac{di_i}{dt} = \frac{v_i - v_{C_f} - R_i \cdot i_i}{L_i} \quad (3.9)$$

Figure 3.8: KVL of the second inductor (L_g) of a LCL filter of a 2-level 3-phase inverter.

$$v_{C_f} - v_{L_g} - v_g = 0$$

$$v_{L_g} = \frac{di_g}{dt} \cdot L_g + R_g \cdot i_g$$

$$\dot{i}_g = \frac{di_g}{dt} = \frac{v_{C_f} - v_g - R_g \cdot i_g}{L_g} \quad (3.10)$$

State Space

After equations 3.8, 3.9, and 3.10 are applied to the a , b , and c phases, the state-space representation in Equation (3.11) is obtained. Similarly as in the derivation of the L filter, the \mathbf{B} matrix is divided in \mathbf{B}_1 and \mathbf{B}_2 and the \mathbf{U} vector into \mathbf{U}_1 and \mathbf{U}_2 , with the objective of using v_i as control input when deriving the transfer function.

$$\begin{aligned}
\dot{\mathbf{X}} = \mathbf{A} \mathbf{X} + \mathbf{B}_1 \mathbf{U}_1 + \mathbf{B}_2 \mathbf{U}_2
\end{aligned}
\quad (3.11)$$

where

$$\mathbf{A} = \begin{bmatrix}
-\frac{R_i}{L_i} & 0 & 0 & 0 & 0 & 0 & -\frac{1}{L_i} & 0 & 0 \\
0 & -\frac{R_i}{L_i} & 0 & 0 & 0 & 0 & 0 & -\frac{1}{L_i} & 0 \\
0 & 0 & -\frac{R_i}{L_i} & 0 & 0 & 0 & 0 & 0 & -\frac{1}{L_i} \\
0 & 0 & 0 & -\frac{R_g}{L_g} & 0 & 0 & \frac{1}{L_g} & 0 & 0 \\
0 & 0 & 0 & 0 & -\frac{R_g}{L_g} & 0 & 0 & \frac{1}{L_g} & 0 \\
0 & 0 & 0 & 0 & 0 & -\frac{R_g}{L_g} & 0 & 0 & \frac{1}{L_g} \\
\frac{1}{C_f} & 0 & 0 & -\frac{1}{C_f} & 0 & 0 & 0 & 0 & 0 \\
0 & \frac{1}{C_f} & 0 & 0 & -\frac{1}{C_f} & 0 & 0 & 0 & 0 \\
0 & 0 & \frac{1}{C_f} & 0 & 0 & -\frac{1}{C_f} & 0 & 0 & 0
\end{bmatrix}$$

$$\mathbf{B}_1 = \begin{bmatrix} \frac{1}{L_i} & 0 & 0 \\ 0 & \frac{1}{L_i} & 0 \\ 0 & 0 & \frac{1}{L_i} \end{bmatrix}$$

$$\mathbf{B}_2 = \begin{bmatrix} -\frac{1}{L_g} & 0 & 0 \\ 0 & -\frac{1}{L_g} & 0 \\ 0 & 0 & -\frac{1}{L_g} \end{bmatrix}$$

$$\mathbf{U}_1 = \begin{bmatrix} v_{ia} \\ v_{ib} \\ v_{ic} \end{bmatrix}, \quad \mathbf{U}_2 = \begin{bmatrix} v_{ga} \\ v_{gb} \\ v_{gc} \end{bmatrix}$$

$$\mathbf{X} = \begin{bmatrix} i_{ia} \\ i_{ib} \\ i_{ic} \\ i_{ga} \\ i_{gb} \\ i_{gc} \\ v_{Cfa} \\ v_{Cfb} \\ v_{Cfc} \end{bmatrix}$$

$$\mathbf{Y} = \mathbf{C} \mathbf{X} + \mathbf{D} \mathbf{U}
\quad (3.12)$$

where

$$\mathbf{C} = \begin{bmatrix} 0 & 0 & 0 & 1 & 0 & 0 & 0 & 0 & 0 \\ 0 & 0 & 0 & 0 & 1 & 0 & 0 & 0 & 0 \\ 0 & 0 & 0 & 0 & 0 & 1 & 0 & 0 & 0 \end{bmatrix}$$

$$\mathbf{D} = \begin{bmatrix} 0 \\ 0 \\ 0 \end{bmatrix}$$

$$\mathbf{U} = \begin{bmatrix} v_{ia} \\ v_{ib} \\ v_{ic} \\ v_{ga} \\ v_{gb} \\ v_{gc} \end{bmatrix}$$

$$\mathbf{Y} = \begin{bmatrix} i_{ga} \\ i_{gb} \\ i_{gc} \end{bmatrix}$$

Transfer function

The transfer function is obtained from the state-space Equations 3.11 and 3.12. Equation (3.13) presents the obtained result.

$$H(s) = \frac{i_g(s)}{v_i(s)} = \frac{1}{(C_f L_i L_g) s^3 + C_f (L_g R_i + L_i R_g) s^2 + (L_i + L_g + C_f R_i R_g) s + R_i + R_g} \quad (3.13)$$

In case of omitting the resistance of the inductors, the resulting transfer function is presented in Equation (3.14).

$$H(s) = \frac{i_g(s)}{v_i(s)} = \frac{1}{(C_f L_i L_g) s^3 + (L_i + L_g) s} \quad (3.14)$$

***dq*-frame**

Translated to *dq* frame the State Space is shown in Equations 3.15 and 3.16.

$$\begin{aligned} \dot{\mathbf{X}} = \mathbf{A} \mathbf{X} + \mathbf{B}_1 \mathbf{U}_1 + \mathbf{B}_2 \mathbf{U}_2 \end{aligned} \quad (3.15)$$

$$\begin{aligned} \begin{bmatrix} \dot{i}_{iq} \\ \dot{i}_{id} \\ \dot{i}_{gq} \\ \dot{i}_{gd} \\ \dot{v}_{Cfq} \\ \dot{v}_{Cfd} \end{bmatrix} &= \begin{bmatrix} -\frac{R_i}{L_i} & -\omega & 0 & 0 & \frac{-1}{L_i} & 0 \\ \omega & -\frac{R_i}{L_i} & 0 & 0 & 0 & \frac{-1}{L_i} \\ 0 & 0 & -\frac{R_g}{L_g} & -\omega & \frac{1}{L_g} & 0 \\ 0 & 0 & \omega & -\frac{R_g}{L_g} & 0 & \frac{1}{L_g} \\ \frac{1}{C_f} & 0 & \frac{-1}{C_f} & 0 & 0 & -\omega \\ 0 & \frac{1}{C_f} & 0 & \frac{-1}{C_f} & \omega & 0 \end{bmatrix} \begin{bmatrix} i_{iq} \\ i_{id} \\ i_{gq} \\ i_{gd} \\ v_{Cfq} \\ v_{Cfd} \end{bmatrix} + \begin{bmatrix} \frac{1}{L_i} & 0 \\ 0 & \frac{1}{L_i} \end{bmatrix} \begin{bmatrix} v_{iq} \\ v_{id} \end{bmatrix} + \begin{bmatrix} \frac{-1}{L_g} & 0 \\ 0 & \frac{-1}{L_g} \end{bmatrix} \begin{bmatrix} v_{gq} \\ v_{gd} \end{bmatrix} \end{aligned}$$

$$\mathbf{Y} = \mathbf{C} \mathbf{X} + \mathbf{D} \mathbf{U} \quad (3.16)$$

$$\begin{bmatrix} i_{gq} \\ i_{gd} \end{bmatrix} = \begin{bmatrix} 0 & 0 & 1 & 0 & 0 & 0 \\ 0 & 0 & 0 & 1 & 0 & 0 \end{bmatrix} \begin{bmatrix} i_{iq} \\ i_{id} \\ i_{gq} \\ i_{gd} \\ v_{Cfq} \\ v_{Cfd} \end{bmatrix} + \begin{bmatrix} 0 \\ 0 \end{bmatrix} \begin{bmatrix} v_{iq} \\ v_{id} \\ v_{gq} \\ v_{gd} \end{bmatrix}$$

3.7 Sizing of Filter Components

In this section component sizes for the operating values presented in Section 2.0.4 are calculated. The inductances are calculated for LCL filter and then the L filter was designed by removing the C, essentially keeping only the series inductance of the LCL.

Grid and Switching Frequencies

The grid frequency (f_0) used is 50 Hz and the switching frequency (f_{sw}) chosen is 5550 Hz, as it is an odd multiple of 3, and significantly larger than, the fundamental frequency.[24].

Base Values

The procedure begins with the calculation of base values for impedance (Z_b) and capacitance (C_b), as shown in Equations 3.17 and 3.18. Filter components are obtained from a

normalised value that indicates the component impedance or capacitance in relation to these base values, expressed as a ratio. This procedure facilitates the design procedure in case of scalability of the system[26, 27, 28].

$$Z_b = \frac{E_n^2}{S_n} = \frac{400^2}{5 \cdot 10^5} = 0.32 \, \Omega \quad (3.17)$$

$$C_b = \frac{1}{\omega_0 \cdot Z_b} = \frac{1}{2\pi \cdot 50 \cdot 0.32} = 9.9 \, \text{mF} \quad (3.18)$$

Capacitor

The calculation is presented in Equation (3.19). The value of the capacitance is limited by the decrease of the power factor, which is chosen to be maximum 5 % when operating at the rated power[29], as presented in Equation (3.19).

$$x = 0.05$$

$$C_f = x \cdot C_b = 0.05 \cdot 9.9 \cdot 10^{-3} = 497 \, \mu\text{F} \quad (3.19)$$

Inverter-Side Inductance

The guiding factor for choosing L_i is how much current ripple should be allowed. The percentage should be limited in the range of 10-25 % of the peak rated output current (\hat{I}_{rated}) as calculated in Equations (3.20) and (3.21), where the bigger value, 25 %, is used to allow a smaller inductor[30, 31].

$$\hat{I}_{rated} = \frac{S_n \cdot \sqrt{2}}{3 \cdot E_{ph}} = \frac{500\,000 \cdot \sqrt{2}}{3 \cdot 400 / \sqrt{3}} = 1\,020.62 \, \text{A} \quad (3.20)$$

$$\Delta_i \leq \frac{\text{Ripple \%}}{100} \cdot \hat{I}_{rated} = 0.25 \cdot 1\,020.62 = 255.15 \, \text{A} \quad (3.21)$$

Using the obtained value and taking other parameters as switching frequency and voltage on the DC side, on Equation (3.22) the calculation for the minimum inductance is presented.

$$L_{i_{MIN}} = \frac{V_{DC}}{8 \cdot f_{sw} \cdot \Delta_i} = \frac{1\,500}{8 \cdot 5\,550 \cdot 255.15} = 0.13 \, \text{mH} \quad (3.22)$$

To improve current tracking capabilities of the converter and avoid large AC voltage drops, the inductance cannot be too large[31, 32]. The upper ceiling for L_i is determined by Equation (3.23).

$$L_{i_{MAX}} = \frac{\sqrt{V_{DC}^2/3 - (E_{ph}\sqrt{2})^2}}{f_{sw} \cdot \hat{I}_{rated}} = \frac{\sqrt{1500^2/3 - (400\sqrt{2}/\sqrt{3})^2}}{2\pi \cdot 50 \cdot 1020.62} = 2.50 \text{ mH} \quad (3.23)$$

Since a smaller inductor usually means a more cost-effective installation, an inductor slightly higher than the minimum is selected and $L_i = 0.14 \text{ mH}$.

Grid-Side Inductor

The filter is designed to achieve a 20 % current ripple attenuation. The attenuation can be increased, although it results in a costlier filter[30].

The desired current ripple reduction is selected then the outer inductor derived. This calculation neglects losses and damping of the filter. The grid-side inductor (L_g) for a ripple attenuation of 20 %

$$\frac{i_g(h_{sw})}{i_i(h_{sw})} = \frac{1}{|1 + r \cdot (1 - L_i \cdot C_b \cdot \omega_{sw}^2 \cdot x)|} \Rightarrow$$

$$0.2 = \frac{1}{|1 + r \cdot (1 - 0.14 \cdot 10^{-3} \cdot 9.9 \cdot 10^{-3} \cdot (2\pi \cdot 5550)^2 \cdot 0.05)|} \Rightarrow r = 0.0467$$

$$L_g = r \cdot L_i = 0.0467 \cdot 0.14 \cdot 10^{-3} = 6.69 \text{ } \mu\text{H} \quad (3.24)$$

Parasitic Resistances

Parasitic resistances of inductors L_i and L_g , denoted as R_i and R_g , are extracted from the manufacturers datasheet of a commercial filter, and are $R_i = 0.7 \text{ m}\Omega$ and $R_g = 0.4 \text{ m}\Omega$ [33].

Resonant Frequency

The resonant frequency (ω_r) should range approximately between ten times the line frequency and half of the switching frequency, to avoid issues in the lower and upper harmonics[29]. With the obtained filter parameters, resonant frequency can be verified as shown in Equations (3.25) and (3.26), confirming that it is approximately half of the switching frequency.

$$\omega_r = \sqrt{\frac{L_i + L_g}{L_i \cdot L_g \cdot C_f}} = \sqrt{\frac{0.14 \cdot 10^{-3} + 6.69 \cdot 10^{-6}}{0.14 \cdot 10^{-3} \cdot 6.69 \cdot 10^{-6} \cdot 497 \cdot 10^{-6}}} = 17735 \text{ rad/s} \quad (3.25)$$

$$f_r = \frac{\omega_r}{2\pi} = \frac{17735}{2\pi} = 2822.6 \text{ Hz} \quad (3.26)$$

The specific values of the components are summarised in Table 3.1.

Table 3.1: Specifications of LCL and L filters

LCL filter	L_i	$1.4338 \cdot 10^{-4} \text{ H}$
	L_g	$6.6909 \cdot 10^{-6} \text{ H}$
	R_i	$0.7 \cdot 10^{-3} \Omega$
	R_g	$0.4 \cdot 10^{-3} \Omega$
	C_f	$497 \cdot 10^{-6} \text{ F}$
L filter	L	$1.5007 \cdot 10^{-4} \text{ H}$
	R	$1.1 \cdot 10^{-3} \Omega$

3.8 Phase-Locked Loop

3.8.1 Primary Analysis

A phase-locked loop is an important part of a grid-connected inverter, as the phase is required for the dq transforms performed in the inverter control loop, keeping the inverter output in phase with the grid. A PLL functions by driving the q term of the three-phase grid voltage to zero[23].

The PLL is set up as shown in Figure 3.9

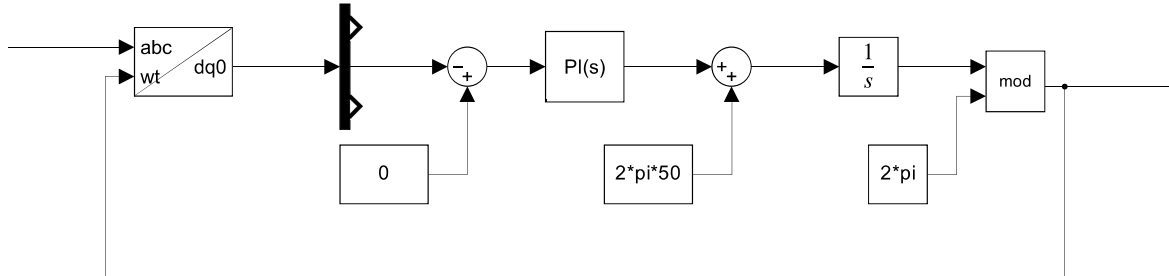
**Figure 3.9:** A diagram of the PLL.

Figure 3.9 comprises of a $dq0$ transform of the grid voltages, of which only the q -term is put forth in the control loop. This is compared to a reference, set to zero, which goes through the controller and outputs the change in angular frequency, $\Delta\omega$. A center frequency of $50 \cdot 2\pi$ radians is added and integrated, which outputs the phase angle θ . The modulo operation constrains the phase angle to the bounds of 0 - 2π . The output is fed back to the $abc/dq0$ transformation block at the input, which means that feedback control techniques can be used to control the loop and drive the q term to zero.

3.8.2 Control

Applying a PI controller to the PLL, The open loop transfer function is given in Equation (3.27), where G is the gain of the dq transform, which is the grid voltage magnitude.

$$H_{OL}(s) = G \cdot \frac{K_p s + K_i}{s} \cdot \frac{1}{s} \quad (3.27)$$

The closed loop then becomes Equation (3.28) as per Mason's rule.

$$H_{CL}(s) = \frac{GK_p s + GK_i}{s^2 + GK_p s + GK_i} \quad (3.28)$$

Comparing Equation (3.28) to the standard form of a second-order transfer function in Equation (3.29), the PI control values can be set to determine the system characteristics with regard to natural frequency and damping ratio.

$$G(s) = \frac{\omega_n^2}{s^2 + 2\zeta\omega_n s + \omega_n^2} \quad (3.29)$$

Setting the damping ratio to the critically damped value of $1/\sqrt{2}$ and the natural frequency to 75 Hz, 50 % higher than the grid frequency in order to tune the controller for a faster response, and with a gain of 230, the controller values are given in Equations (3.30) and (3.31).

$$K_i = \frac{\omega_n^2}{G} = 965.50 \quad (3.30)$$

$$K_p = \frac{2\zeta\omega_n}{G} = 2.8975 \quad (3.31)$$

Testing the PLL with the derived controller values and a 50 Hz grid input in Simulink, Figure 3.10 shows the error signal v_q being driven to zero as expected.

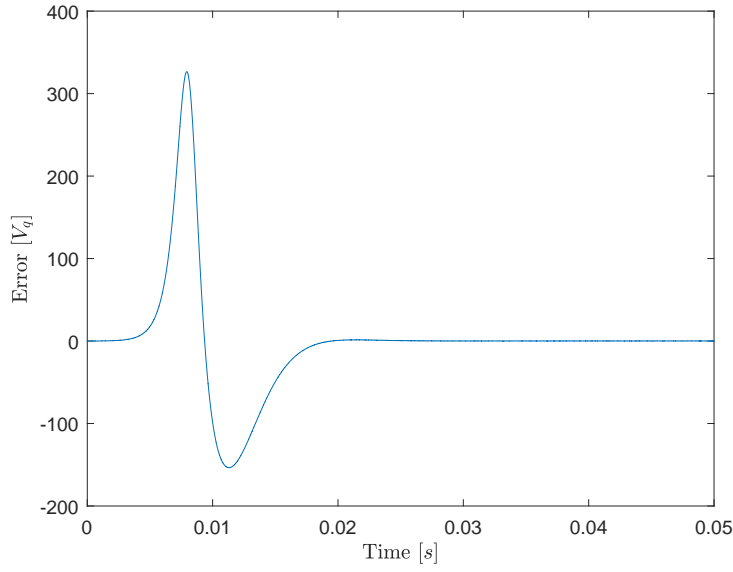


Figure 3.10: A plot showcasing v_q with a 50Hz grid input.

3.9 Control

To regulate the power and current injection to the grid, control loops were designed. Below is a derivation and explanation of how these control structures were implemented based on the mathematical equations describing the filters.

3.9.1 Power Control

The function of the power control subsystem is to calculate the reference current signal that is passed to the current controller such that the power is regulated to the desired set point. In the dq -domain, the power measured at the filter output can in general be described by Equation (3.32) and Equation (3.33)[23].

$$P_g(t) = \frac{3}{2}(v_{gd} \cdot i_{gd}(t) + v_{gq} \cdot i_{gq}(t)) \quad (3.32)$$

$$Q_g(t) = \frac{3}{2}(-v_{gd} \cdot i_{gq}(t) + v_{gq} \cdot i_{gd}(t)) \quad (3.33)$$

Given that the function of the PLL is to drive v_q to zero, and it is assumed it does, the equations can be written with $v_{gq} = 0$ and isolated for $i_{gd}(t)$ and $i_{gq}(t)$.

$$i_{gd}(t) = \frac{2}{3v_{gd}}P_g(t) \quad (3.34)$$

$$i_{gq}(t) = \frac{-2}{3v_{gd}}Q_g(t) \quad (3.35)$$

Setting $P_g(t)$ and $Q_g(t)$ to the desired reference constants, measurement of $V_{gd}(t)$ can yield the reference currents which are passed to the current controller. The Simulink implementation can be found in Appendix B.

3.9.2 Transfer Function Analysis

L Transfer Function

Applying the inductance and resistance from Section 3.7 to the transfer function Equation (3.5), Equation (3.36) is given.

$$H(s) = \frac{1}{1.5007 \cdot 10^{-4}s + 0.0011} \quad (3.36)$$

This transfer function is inherently stable, with a pole at -7.33. This stability is due to the parasitic resistance, as it would otherwise be marginally stable. This is not much of an issue either way, as any proportional gain applied to the transfer function in closed loop moves the pole to the left. For the LCL transfer function the parasitic resistance has a much larger impact on the system in open and closed loop.

LCL Transfer Function

Applying the inductances, capacitance and resistance from Section 3.7 to the transfer functions in Equation (3.13) and Equation (3.14), the transfer functions are shown in Equations (3.37) and (3.38).

$$H_1(s) = \frac{1}{4.768 \cdot 10^{-13}s^3 + 6.204 \cdot 10^{-08}s^2 + 0.0001501s + 0.0011} \quad (3.37)$$

$$H_2(s) = \frac{1}{4.768 \cdot 10^{-13}s^3 + 0.0001501s} \quad (3.38)$$

Open loop stability for the two transfer functions are different, as Equation (3.37) exhibits a stable system due to its left-hand poles, while Equation (3.38) is marginally stable, with poles at the origin. The bode plot for both functions is given in Figure 3.11.

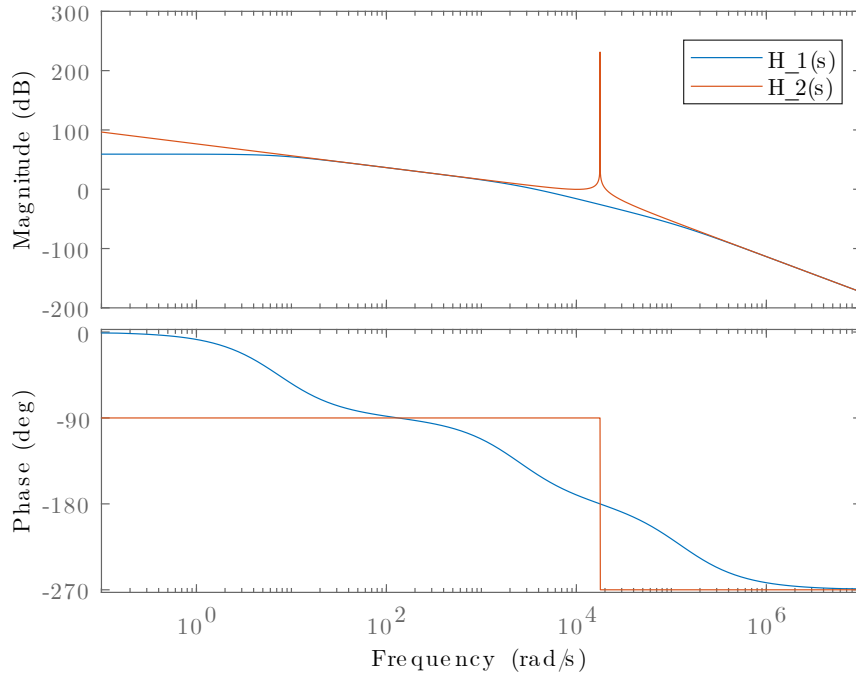


Figure 3.11: A bode plot for the transfer function of the LCL filter with parasitic resistances $H_1(s)$, and without parasitic resistances $H_2(s)$.

It can be seen in Figure 3.11 that the parasitic resistance exhibit a dampening effect of the system, removing the resonant peak present for the frequency response of Equation (3.38). Passive damping is a widely adopted method to guarantee the stability of a voltage source inverter (VSI) based on an LCL filter. Among its advantages, it offers a straightforward, cost-effective[34] implementation with sufficient resonance attenuation. On the other hand, since it requires a physical resistor, relatively high damping losses occur[35, 36, 37, 38]. Damping strategies can be with series or parallel resistors, as well as a combination of both[39, 40]. In this particular model, the representation of the parasitic resistances of the inverter and grid inductors (R_i and R_g) act like a series damping resistor. In this configuration, the higher the resistance the bigger the attenuation of the peak resonance, while a parallel damping resistance would have an inversely proportional effect[41]. As an example of the resistance needed to provide sufficient attenuation, it can be observed in fig. 3.12 that a resistance of 100 m Ω is sufficient to remove the resonant peak.

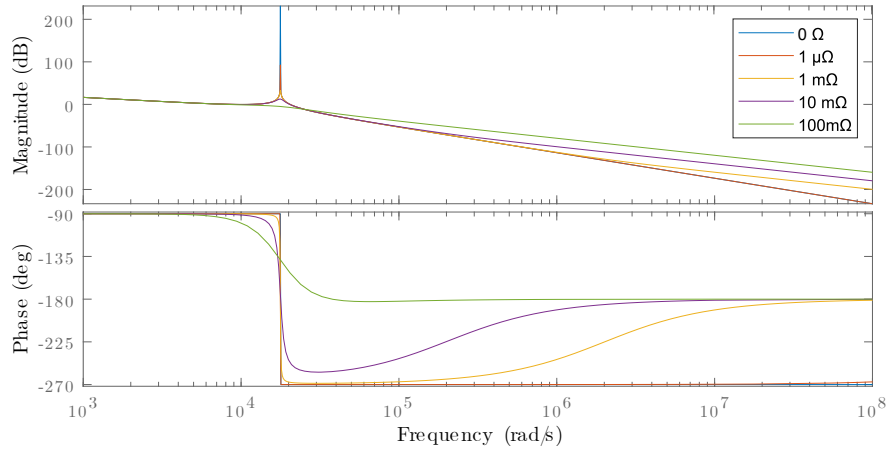


Figure 3.12: A bode plot for H_2S with added series resistance.

3.9.3 PI Current Control

Because the impedance of a capacitor lowers with a rising in frequency of the signal passing, the capacitor will filter out higher frequencies more so than lower ones. This can be observed in Equation (3.39), as ω becomes larger, the impedance becomes smaller.

$$Z_{C_f}(j\omega) = \frac{1}{j\omega C} \quad (3.39)$$

Treating the capacitor as a rather static component which only affects the system in a filtering aspect, a more simple control structure can be derived and designed than that of the derived transfer function for an LCL filter. Disregarding the capacitor, the filter transfer function turns into a first order transfer function describing an L filter. Thus, the control design can be applied to both Equations (3.36) and (3.37).

Applying a PI controller $C(s)$ to the transfer function of an L filter as derived in Equation (3.5) this system yields Equation (3.40).

$$C(s)H_{OL}(s) = \frac{K_p s + K_i}{s} \cdot \frac{1}{Ls + R} = \frac{s + \frac{K_i}{K_p}}{s + \frac{R}{L}} \cdot \frac{K_p}{Ls} \quad (3.40)$$

It can be observed that if the controller values are chosen for the zero correctly, the zero can be cancelled and the open loop gain be described by K_p/Ls . Applying feedback to this, Equation (3.41) arises.

$$H_{CL}(s) = \frac{1}{\frac{L}{K_p}s + 1} \quad (3.41)$$

The time constant of this first order system is described by $\tau = L/K_p$. This relationship can also be used in combination with Equation (3.40) to yield the relationship between the time constant and resistance. To summarize, if the controller values are chosen such that they cancel the pole in Equation (3.40), they can be related to the time constant of the resulting closed loop Equation (3.41) as given in Equation (3.42).

$$K_p = \frac{L}{\tau} \quad (3.42)$$

$$K_i = \frac{R}{\tau} \quad (3.43)$$

The design of the PI controller is thus simplified to one variable instead of two. Ideally, τ would be set as small as possible for a quick response, however it is limited by the bandwidth of the switching frequency, and should be set a below this. τ was thus set to around 1.5 % of the switching time constant, $\frac{1}{2\pi \cdot 5550 \cdot 0.015} \approx 2 \cdot 10^{-3}s$, which is within the recommended range of 0.5-5 ms[23]. This yields controller values of $K_p = \frac{L_i + L_g}{\tau} = 0.075$ and $K_i = \frac{R_i + R_g}{\tau} = 0.55$.

Applying this controller to Equation (3.37) and Equation (3.36), the step response in Figure 3.13 is given.

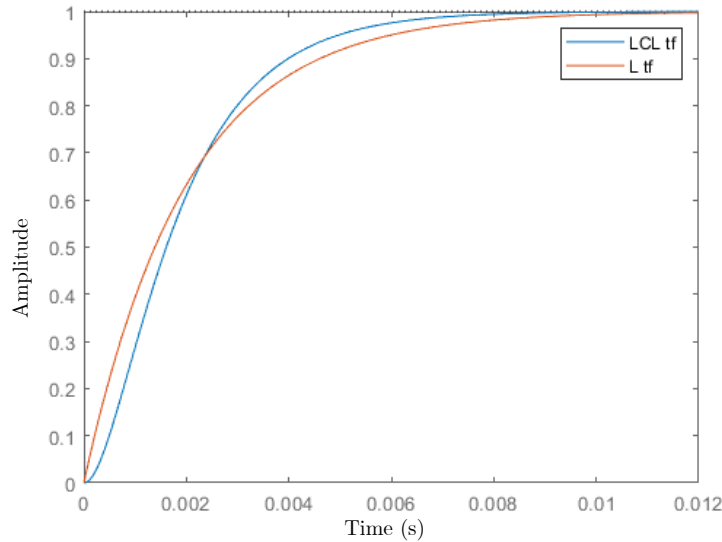


Figure 3.13: A step response of the closed loop LCL and L transfer function with the derived PI controller.

To achieve the desired reference from the controller once implemented in the physical system, disturbances can be fed back to the controller directly which have not been taken into consideration in the controller tuning. The relevant disturbances can be observed in the derived dq -frame state space equations in Equation (3.6).

Assuming a steady state, the inverter voltages v_{id} and v_{iq} can be described by re-arranging the equations in Equation (3.6).

$$v_{id} = -L \cdot \omega_0 \cdot i_{gq} + R \cdot i_{gd} + v_{gd} \quad (3.44)$$

$$v_{iq} = L \cdot \omega_0 \cdot i_{gd} + R \cdot i_{gq} + v_{gq} \quad (3.45)$$

Measuring and feeding these values to the output of the controller thus minimises the required disturbance rejection required by the controller. The Matlab code used to calculate these values is given in Appendix A. The structure of the controller in Simulink can be found in Appendix B.

3.9.4 State-Space Current Control

L filter

While the same PI controller functioned both for the LCL and L transfer functions, this was not the case for state-space control, thus two separate control derivations were made for the LCL and L models.

Applying the component sizes from Section 3.7, the state-space description Equation (3.46) is obtained.

$$\dot{\mathbf{X}} = \begin{bmatrix} 314.1593 & -7.2998 \\ -7.2998 & -314.1593 \end{bmatrix} \begin{bmatrix} i_{gd} \\ i_{gq} \end{bmatrix} + \begin{bmatrix} 6.6361 \cdot 10^3 & 0 \\ 0 & 6.6361 \cdot 10^3 \end{bmatrix} \begin{bmatrix} v_{gd} \\ v_{gq} \end{bmatrix} \quad (3.46)$$

$$\mathbf{C} = \begin{bmatrix} 1 & 0 \\ 0 & 1 \end{bmatrix} \begin{bmatrix} i_d \\ i_q \end{bmatrix} \quad (3.47)$$

To control the state space system via full state feedback, the Linear Quadratic Regulator (LQR) method was applied. LQR works by solving a cost function where values can be assigned to weight the cost of error allowance in the output, versus the control effort required to achieve said error. This involves the matrix \mathbf{Q} , which emphasises the cost of error of the states, and \mathbf{R} which weights the cost of controller effort[42]. As the control

will be implemented in simulation there is no restriction on control effort, and emphasis is put on state error minimisation. The \mathbf{Q} and \mathbf{R} matrices are thus given in Equation (3.48) and Equation (3.49).

$$\mathbf{Q} = \begin{bmatrix} 100 & 0 \\ 0 & 100 \end{bmatrix} \quad (3.48)$$

$$\mathbf{R} = 1 \quad (3.49)$$

Using the LQR function of Matlab to solve the cost function for feedback matrix \mathbf{K} , the matrix in Equation (3.50) is given.

$$\mathbf{K} = \begin{bmatrix} 10.0475 & -0.0011 \\ -0.0011 & 9.9528 \end{bmatrix} \quad (3.50)$$

Although this system is stable, with two poles at $-6.66 \cdot 10^4$, reference tracking needs to be added. The reference tracking applied to the system amounts to solving Equation (3.51)[43].

$$\begin{bmatrix} \mathbf{A} & \mathbf{B} \\ \mathbf{C} & \mathbf{D} \end{bmatrix} \begin{bmatrix} \mathbf{N}_x \\ N_u \end{bmatrix} = \begin{bmatrix} 0 \\ \vdots \\ 1 \end{bmatrix} \quad (3.51)$$

The \mathbf{A} , \mathbf{B} , \mathbf{C} , and \mathbf{D} matrices are those describing the system, while \mathbf{N}_x is a reference gain applied to the state feedback and N_u are gains applied to the reference input to the system. These reference gains can be grouped together from $u = N_u r - \mathbf{K}(\mathbf{x} - \mathbf{N}_x)r$ to $u = -\mathbf{K}\mathbf{x} + \bar{N}r$. Solving for the reference gain results in $\bar{N} = 10.0944$.

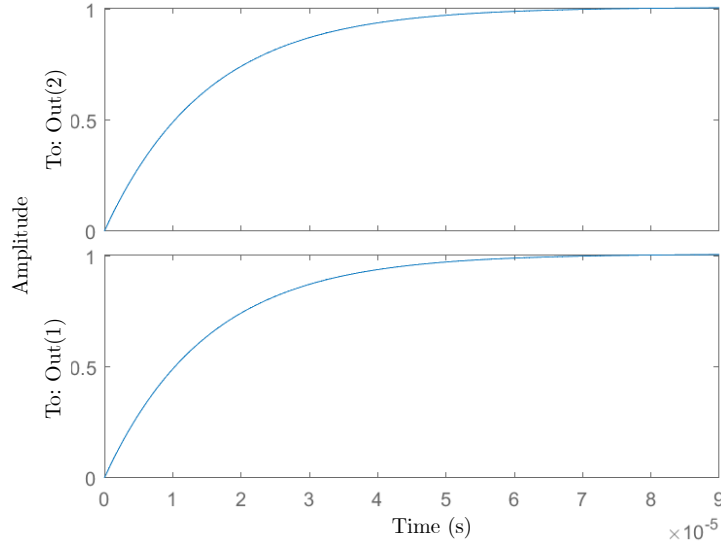


Figure 3.14: Step response of the controlled L filter state space model, with output I_{gd} and I_{gq} .

The Matlab code used to calculate these values is given in Appendix A. The structure of the controller in Simulink can be found in Appendix B.

LCL Filter

A reorganised equation of the state-space model of the LCL model from Equation (3.15) is used, where the grid voltage and current coupling are considered as internal disturbances and separated out of the **A** and **B** matrices. Furthermore, the d and q terms can be separated[44]. This yields the d side state-space Equation (3.52).

$$\dot{\mathbf{X}} = \begin{bmatrix} -\frac{R_i}{L_i} & 0 & -\frac{1}{L_i} \\ 0 & -\frac{R_g}{L_g} & \frac{1}{L_g} \\ \frac{1}{C_f} & -\frac{1}{C_f} & 0 \end{bmatrix} \begin{bmatrix} i_{id} \\ i_{gd} \\ v_{C_f d} \end{bmatrix} + \begin{bmatrix} \frac{1}{L_i} \\ 0 \\ 0 \end{bmatrix} v_i + \begin{bmatrix} 0 \\ -\frac{1}{L_g} \\ 0 \end{bmatrix} v_g + \omega \begin{bmatrix} i_{iq} \\ i_{gq} \\ v_{C_f q} \end{bmatrix} \quad (3.52)$$

$$\mathbf{Y} = \begin{bmatrix} 0 & 1 & 0 \end{bmatrix} \begin{bmatrix} i_{id} \\ i_{gd} \\ v_{C_f d} \end{bmatrix} \quad (3.53)$$

On the q side, Equation (3.54) is given.

$$\dot{\mathbf{X}} = \begin{bmatrix} -\frac{R_i}{L_i} & 0 & -\frac{1}{L_i} \\ 0 & -\frac{R_g}{L_g} & \frac{1}{L_g} \\ \frac{1}{C_f} & -\frac{1}{C_f} & 0 \end{bmatrix} \begin{bmatrix} i_{iq} \\ i_{gq} \\ v_{C_fq} \end{bmatrix} + \begin{bmatrix} \frac{1}{L_i} \\ 0 \\ 0 \end{bmatrix} v_i + \begin{bmatrix} 0 \\ -\frac{1}{L_g} \\ 0 \end{bmatrix} v_g - \omega \begin{bmatrix} i_{id} \\ i_{gd} \\ v_{C_fd} \end{bmatrix} \quad (3.54)$$

$$\mathbf{Y} = \begin{bmatrix} 0 & 1 & 0 \end{bmatrix} \begin{bmatrix} i_{iq} \\ i_{gq} \\ v_{C_fq} \end{bmatrix} \quad (3.55)$$

It can be observed that the only difference is the coupling term. Since this is to be treated as a disturbance, the control can be developed for the d side only, and applied to d and q control independently.

Applying the component sizes found in Section 3.7, we get the following \mathbf{A} and \mathbf{B} matrices in Equation (3.56).

$$\dot{\mathbf{X}} = \begin{bmatrix} -4.8611 & 0 & -6.9444 \cdot 10^3 \\ 0 & -59.7907 & 1.4948 \cdot 10^5 \\ 2.0121 \cdot 10^3 & -2.0121 \cdot 10^3 & 0 \end{bmatrix} \begin{bmatrix} i_{id} \\ i_{gd} \\ v_{C_fd} \end{bmatrix} + \begin{bmatrix} 6.9444 \cdot 10^3 \\ 0 \\ 0 \end{bmatrix} v_i \quad (3.56)$$

The system has three poles, all located on the y axis, making the system marginally stable. It is thus necessary to apply control techniques.

As for the L filter, the LQR method of control is implemented for the LCL filter. Since the system has three states, and the one of ultimate interest is i_{gd} , emphasis is put on this state in the \mathbf{Q} matrix. For simulation purposes, controller effort is not of primary concern and thus R is set to 1. The applied \mathbf{Q} and \mathbf{R} matrices are given in Equation (3.57) and Equation (3.58).

$$\mathbf{Q} = \begin{bmatrix} 1 & 0 & 0 \\ 0 & 100 & 0 \\ 0 & 0 & 1 \end{bmatrix} \quad (3.57)$$

$$R = 1 \quad (3.58)$$

Solving the cost function for feedback matrix \mathbf{K} , the matrix in Equation (3.59) is given.

$$\mathbf{K} = \begin{bmatrix} 6.8921 & 3.1244 & 80.6100 \end{bmatrix} \quad (3.59)$$

The resulting poles with this feedback matrix are $-2.42 \cdot 10^4$ and $-1.19 \cdot 10^4 \pm 2.69 \cdot 10^4 i$, meaning it is stable. Solving for the reference gain results in $\bar{N} = 10.0499$. Applying the derived values to the system, the step response is given in Figure 3.15.

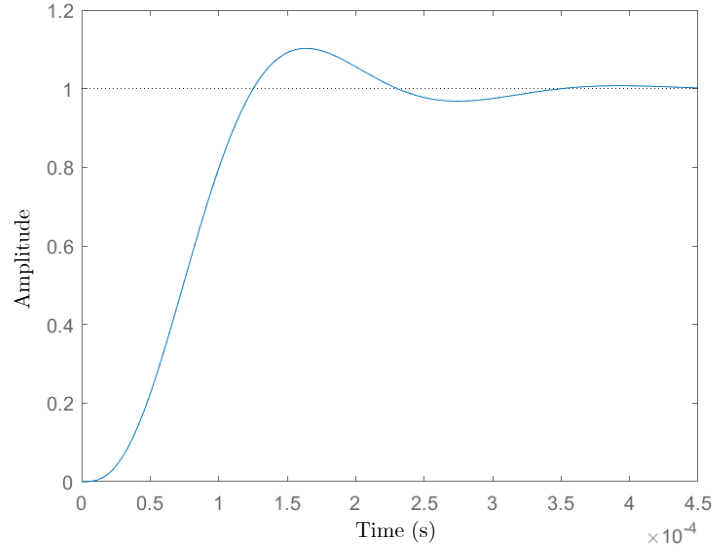


Figure 3.15: A figure of the step response of the controlled state space LCL system.

The Matlab code used to calculate these values is given in Appendix A. The structure of the controller in Simulink can be found in Appendix B.

Table 3.2: Closed loop controlled system characteristics.

	Pole	Damping	ω_n (rad/s)
PI L	-7.33	1.00	7.33
	$-5.00 \cdot 10^2$	1.00	$5.00 \cdot 10^2$
PI LCL	-7.33	1.00	7.33
	$-7.09 \cdot 10^2$	1.00	$7.09 \cdot 10^2$
	$-1.74 \cdot 10^3$	1.00	$1.74 \cdot 10^3$
	$-1.28 \cdot 10^5$	1.00	$1.28 \cdot 10^5$
SS L	$-6.66 \cdot 10^4$	1.00	$6.66 \cdot 10^4$
	$-6.66 \cdot 10^4$	1.00	$6.66 \cdot 10^4$
SS LCL	$-2.42 \cdot 10^4$	1.00	$2.42 \cdot 10^4$
	$-1.19 \cdot 10^4 + 2.69 \cdot 10^4 i$	0.405	$2.95 \cdot 10^4$
	$-1.19 \cdot 10^4 - 2.69 \cdot 10^4 i$	0.405	$2.95 \cdot 10^4$

Observing the step responses and poles for the closed loop PI L and SS L situations, the responses are very similar, though the state space control has a faster settling time, as seen in the natural frequency of the dominant poles. The SS LCL control shows some overshoot due to the lower damping ratio.

Chapter 4

Simulation

This chapter covers the application of the derived PI and state-space controllers to a three-phase inverter circuit built in Simulink. The main aim is to compare the performance to the harmonic requirements for Denmark's DK1 grid presented in Section 2.0.1 with each of the control techniques and filter combinations. The full system build in Simulink can be found in Appendix B.

Methodology

The testing of the system was split up into two sections, corresponding to the two main measurements. These two sections aim to test the systems for the following:

- Testing the reference tracking and bidirectional power flow capabilities.
- Measuring the THD and DC injection to the grid.

The grid resistance (R_{grid}) and inductance (L_{grid}) are set to zero in the simulation, representing a robust grid scenario.

4.1 Reference Tracking

This section displays the testing done for each controller and filter type to determine the reference tracking and bidirectional power flow capability. The test cases for each were performed at set points of 500 kW / 0 VAr and -500 kW / 0 VAr, corresponding to power injection to the grid and power absorption from the grid. Successful reference tracking

here is defined to be an average settling point within 5 % of set point, and with an average ripple no larger than 10 %. The averages are derived from data taken between 0.05-0.1 seconds of simulation start. As such, the expected settling time should be 0.05 seconds.

4.1.1 L Filter

PI Controller

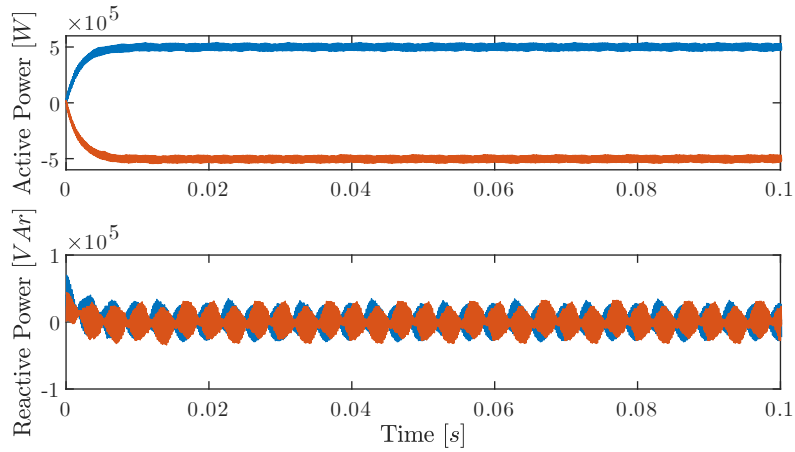


Figure 4.1: The stable active and reactive power output to the grid using PI control at a set point of 500 kW / 0 VAr (blue) and -500 kW / 0 VAr (orange).

The system response in Figure 4.1 shows that it successfully settles at the given set point with an average of 490 kW and an average ripple of ± 26 kW, or 5.3%.

State Space Controller

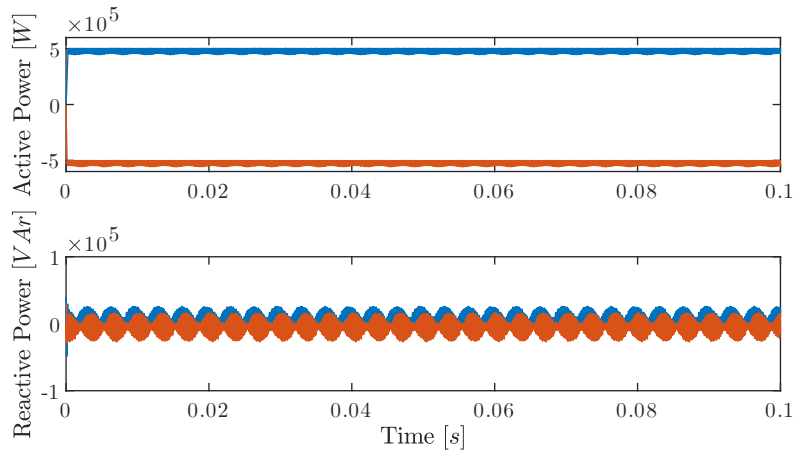


Figure 4.2: The stable active and reactive power output to the grid using PI control at a set point of 500 kW / 0 VAr (blue) and -500 kW / 0 VAr (orange).

The system response in Figure 4.2 shows that it successfully settles at the given set point with an average of 478 kW and an average ripple of ± 13 kW.

4.1.2 LCL Filter

Initial tests with both controller types with the LCL filter gave unstable outputs for a variety of power set points. An example is given in Figure 4.3.

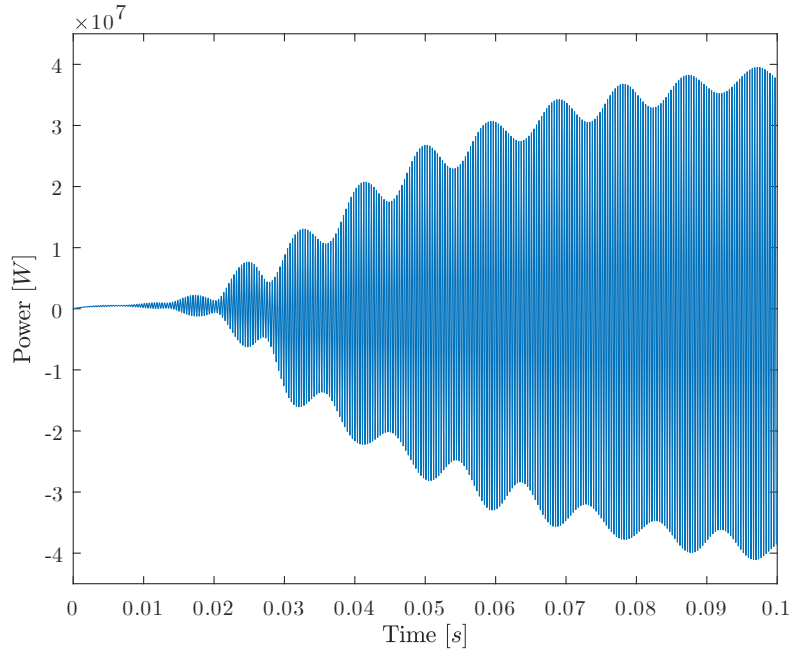


Figure 4.3: The unstable grid power output using the power and PI controller at a set point of 500 kW / 0 VAR.

From Figure 3.11 it was expected that the parasitic resistance provided by the inductors would sufficiently dampen the resonance, though this is shown in Figure 4.3 to not be so. In order to deal with this issue there were several options. As described in Section 3.9.2, tuning damping resistors can be done to deal with this issue, however this solution will cause power losses. Furthermore, given the fact that the stability of the transfer function model did not correspond with the stability in the circuit simulation, to an extent the finding of a sufficient damping resistor would need to be experimental, as the parasitic resistance did not sufficiently dampen the system as expected from the transfer function. It was decided to implement a notch filter, which is capable of filtering out narrow bands of frequencies. The general transfer function of a notch filter is given in Equation (4.1)[45].

$$H_{Notch}(s) = \frac{s^2 + 2 \cdot g \cdot \zeta \cdot \omega_r \cdot s + \omega_r^2}{s^2 + 2 \cdot \zeta \cdot \omega_r \cdot s + \omega_r^2} \quad (4.1)$$

In order to design the filter, it is necessary to know the resonant frequency of the filter, which is given in Section 3.7. The remaining terms are design parameters:

- $g = 2.8184 \cdot 10^{-12}$, corresponding to the inverse of the gain peak of 231 dB seen for Equation (3.38) in Figure 3.11.
- $\zeta = 1$, the damping ratio.

- $\omega_r = 1.7735 \cdot 10^4$, the resonance frequency of the filter.

The final notch filter transfer function is given in Equation (4.2).

$$H_{Notch}(s) = \frac{s^2 + 9.997 \cdot 10^{-8}s + 3.145 \cdot 10^8}{s^2 + 35470s + 3.145 \cdot 10^8} \quad (4.2)$$

Figure 4.4 shows that the notch filter may have the capacity to cancel out the resonance peak of the LCL filter.

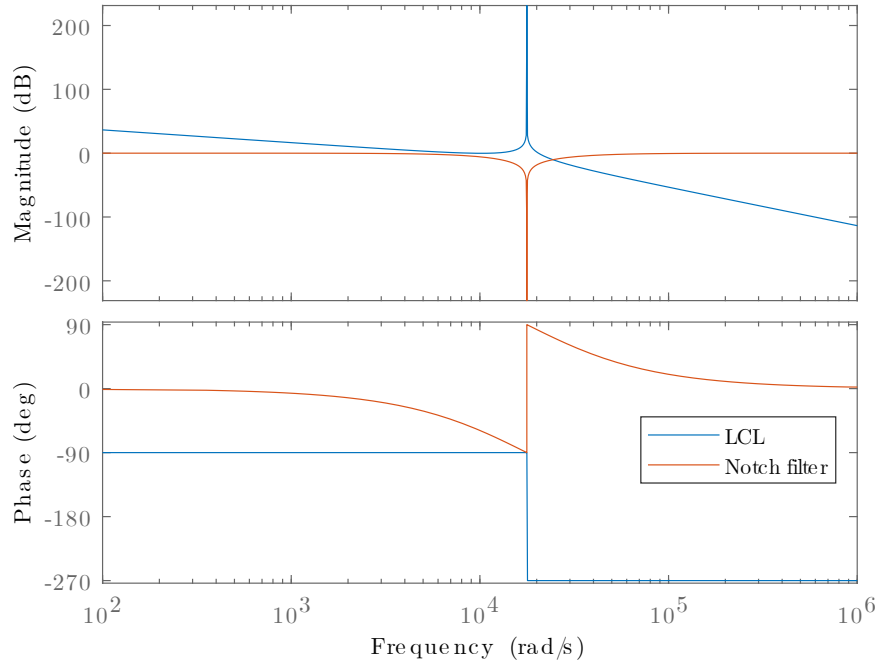


Figure 4.4: A bode plot showing the frequency response of Equation (4.1) and Equation (3.38).

The notch filter was subsequently applied to all feedback of the states in LCL related testing.

PI Controller

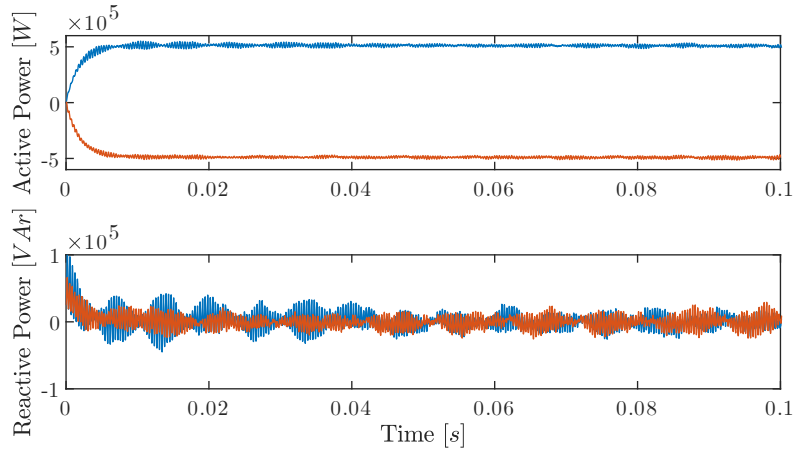


Figure 4.5: The stable active and reactive power output to the grid using PI control at a set point of 500 kW / 0 VAr (blue) and -500 kW / 0 VAr (orange).

The system response in Figure 4.5 shows that it successfully settles at the given set point with an average of 502 kW and an average ripple of ± 20 kW.

State Space Controller

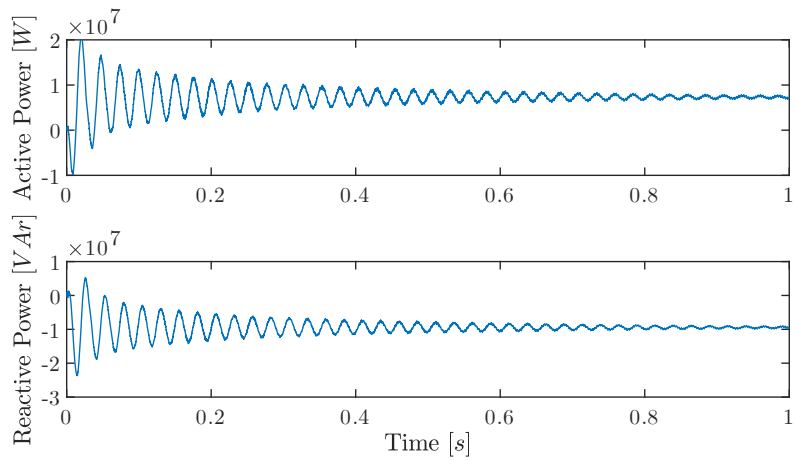


Figure 4.6: The stable active and reactive power output to the grid using state space control at a set point of 500 kW / 0 VAr (blue).

It can be observed in Figure 4.6 that the state space controller was unable to settle the system in the required time, nor at the correct set point. Further testing and manual

tuning of the controller did not significantly improve the results.

4.2 Harmonic Distortion

In this section, THD and DC injection is measured. Measurements were taken between 1.4-2.0 seconds of simulation time and derived using the Simulink FFT Analyzer tool. The measurements are compared to the upper and lower bound requirements for grid connection mentioned in Section 2.0.1.

Table 4.1: THD and DC injection compared to DK1 requirements.

	SCR	THD	DC injection
For SCR rating	≥ 350	18	0.5
DK1 strictest	-	4.4	0.5
PI L	10^{13}	4.05	0.031
SS L	10^{13}	3.23	0.0017
PI LCL	10^{13}	4.11	0.0044
SS LCL	10^{13}	1.46	0.030

Table 4.2: Harmonic distortion of the 15 first harmonics compared to DK1 requirements.

	SCR	Odd harmonic order h							Even harmonic order h					
		3	5	7	9	11	13	15	2	4	6	8	10	12
For SCR rating	≥ 350	7.5	15.0	9.5	1.6	5.7	3.7	1.0	0.5	0.5	1.0	0.8	0.6	0.5
DK1 strictest	-	3.4	3.8	2.5	0.5	1.2	0.7	0.35	0.5	0.5	1.0	0.8	0.6	0.5
PI L	10^{13}	0.51	0.37	0.13	0.25	0.11	0.19	0.033	0.0033	0.015	0.022	0.012	0.0041	0.012
SS L	10^{13}	0.010	0.16	0.070	0.023	0.015	0.018	0.0066	0.012	0.016	0.025	0.020	0.015	0.015
PI LCL	10^{13}	0.29	0.27	0.11	0.16	0.078	0.24	0.071	0.0055	0.014	0.017	0.0043	0.0011	0.026
SS LCL	10^{13}	0.0031	1.27	0.11	0.00080	0.49	0.36	0.00055	0.0029	0.0031	0.00064	0.0016	0.00028	0.011

From Table 4.1 and Table 4.2 it can be seen that all four tests fulfill the stricter regulations around THD and DC injection required for grid connection in Denmark.

An interesting point besides observing the harmonics specified in Table 4.2, are which harmonics are the largest source of distortion for each test. Table 4.3 shows which frequencies make up the largest harmonic distortion for each test.

Table 4.3: Showcases which individual harmonics were the largest source of distortion for each test.

	Distortion Rank				
	1	2	3	4	5
PI L	5 450	5 650	150	250	450
SS L	5 450	5 650	5 750	5 350	250
PI LCL	2 850	2 801.67	2 750	2 798.33	2 848.33
SS LCL	250	550	650	10	8.33

Given that the state space controller was unable to fulfil reference tracking requirements when using the LCL filter, it will not be considered further in the report. The remaining tests will be conducted only with the PI LCL configuration.

4.3 Grid Stiffness Test

In previous tests, a very strong grid was assumed, represented in the simulation by a grid block with zero resistance and inductance. Stability of grid-tied inverters is an important concern for the industry, given that a weak grid can lead to voltage fluctuations at the inverter terminals and cause its instability[46]. In order to determine the response of the system under less ideal conditions, a weaker grid is represented changing the resistance and reactance of the grid block.

As a weak grid is characterised by a smaller short-circuit ratio (SCR)[47], The procedure is to find the corresponding resistance (R_{grid}) and inductance (L_{grid}) values for a given SCR. First, the short circuit power needs to be determined as in Equation (4.3), where the grid inductance ($|Z_{grid}|$) is presented in Equation (4.4).

$$S_{SC} = \frac{E_N^2}{|Z_{grid}|} \quad (4.3)$$

$$|Z_{grid}| = \sqrt{R_{grid}^2 + (2\pi \cdot f_0 \cdot L_{grid})^2} \quad (4.4)$$

The short-circuit ratio is defined as in Equation (4.5). Since the grid voltage is considered low voltage, the impedance is mainly resistive[47][48], therefore the ratio in Equation (4.6) is assumed.

$$SCR = \frac{S_{SC}}{S_N} \quad (4.5)$$

$$R_{grid} = 2 \cdot L_{grid} \quad (4.6)$$

Including the known variables, the SCR is presented in Equation (4.7). Finally, solving for R_{grid} and then calculating L_{grid} can be obtained with Equation (4.8).

$$SCR = \frac{400^2}{\sqrt{R_{grid} + (2\pi \cdot 50 \cdot R_{grid}/2)^2 \cdot 500\,000}} \quad (4.7)$$

$$R_{grid} = \frac{2\,037.14 \cdot 10^{-6}}{SCR} \quad , \quad L_{grid} = \frac{R_{grid}}{2} \quad (4.8)$$

With this configuration a number of simulations calculations were ran based on the DK1 brackets for SCR values presented in Table 2.3. The rate of change for the THD demonstrates a rapid shift between an SCR of 139 and 185 where it transitioned from not complying even with the higher threshold to satisfy the strictest THD of DK1. An additional simulation is then run for a midway value, SCR of 160, which is found to have higher THD than the threshold. The configuration, is therefore not achieving the required performance

This behaviour can also be observed in Figures 4.7, 4.8, and 4.9. While in all of them active power fluctuates at 500 kW and reactive power does it around 0 VAR, as intended, a lower SCR implies higher fluctuations.

Table 4.4: Distortion values of different SCR configurations.

SCR	R_{grid}, L_{grid}		THD	DK1 Threshold THD	DK1 Strictest THD
139	$1.47 \cdot 10^{-5} \Omega$	$7.33 \cdot 10^{-6} \text{ H}$	30.43	$SCR \geq 120 \text{ and } \leq 250$ 8.4	4.4
160	$1.27 \cdot 10^{-5} \Omega$	$6.37 \cdot 10^{-6} \text{ H}$	9.45		
185	$1.10 \cdot 10^{-5} \Omega$	$5.51 \cdot 10^{-6} \text{ H}$	3.91		

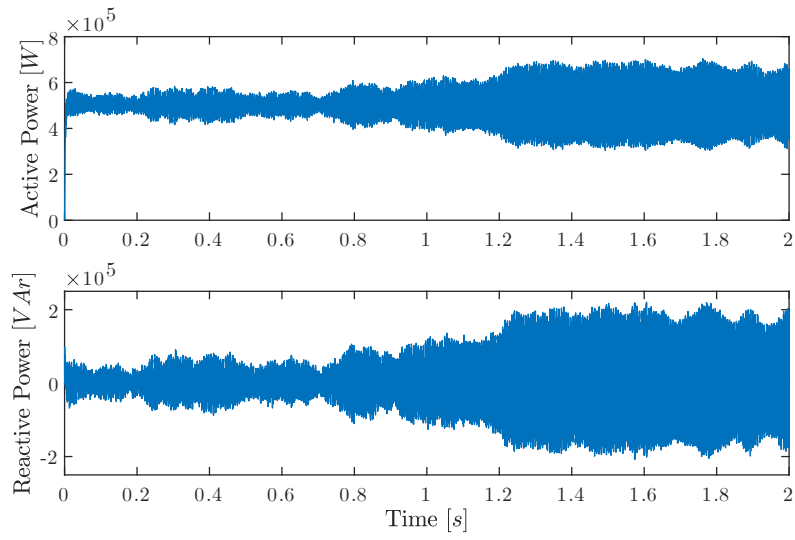


Figure 4.7: Active and reactive power output to the grid for PI LCL configuration with a grid SCR of 139

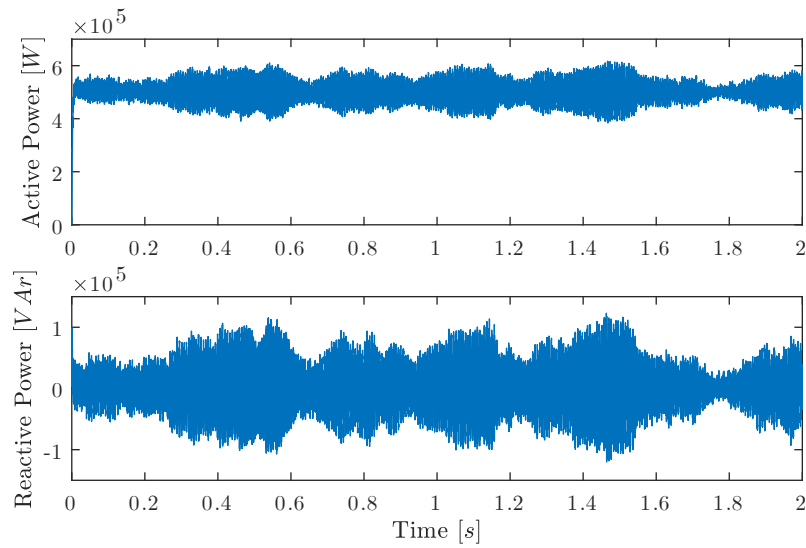


Figure 4.8: Active and reactive power output to the grid for LCL/PI configuration with a grid SCR of 160

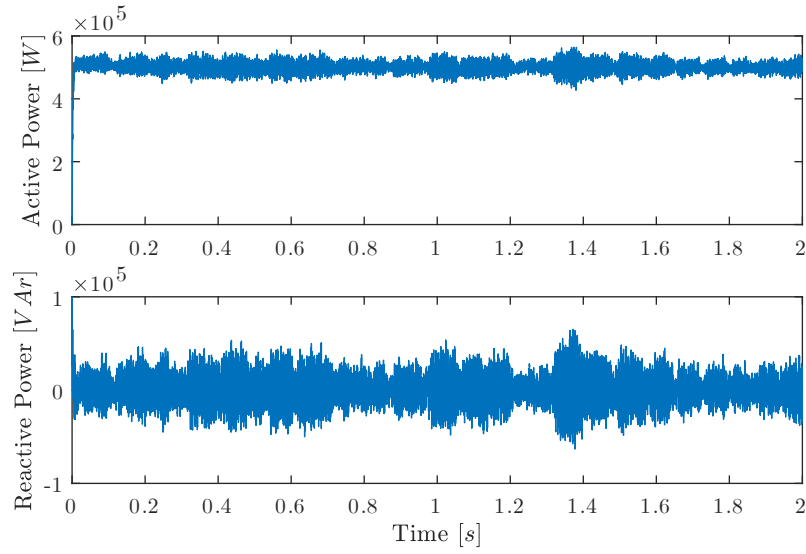


Figure 4.9: Active and reactive power output to the grid for LCL/PI configuration with a grid SCR of 185

4.4 Line Fault Test

For the line fault test a single line-to-ground fault occurs when the PI LCL system configuration is set to inject 500 kW and 0 VAR to the grid. Phase a is disconnected from the grid and shorted to ground at the time when the phase voltage is zero, and in another test when it peaks. Lastly, a test is run to observe the recovery of the system after reconnecting the grid. The schematic of the fault is shown in Figure 4.10.

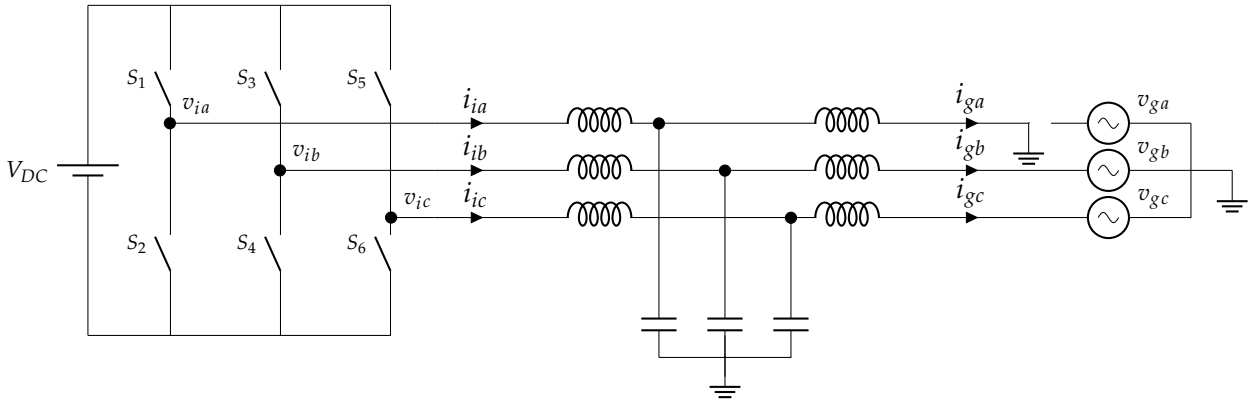


Figure 4.10: Circuit diagram of line-to-ground fault on phase a .

4.4.1 Original PI Controller

Line Fault at Zero Phase Voltage

For this test, the line short happens 0.05 s after the system starts, when the phase voltage is zero. Voltage and current plots using the original PI controller ($K_p = 0.075$, $K_i = 0.55$) are shown in Figure 4.11 and the power injected to the grid is shown in Figure 4.12.

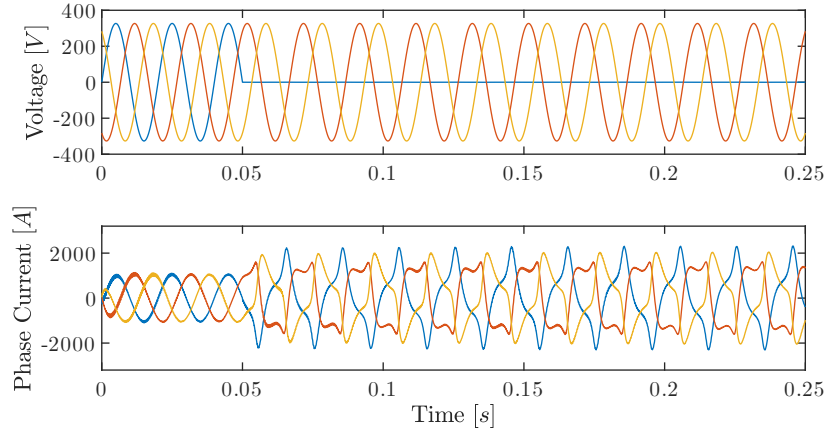


Figure 4.11: v_g and i_g using the original PI controller, short at $t = 0.05$ s. Peak currents: $i_{ga} = 2.3$ kA, $i_{gb} = 1.6$ kA, $i_{gc} = 2.0$ kA.

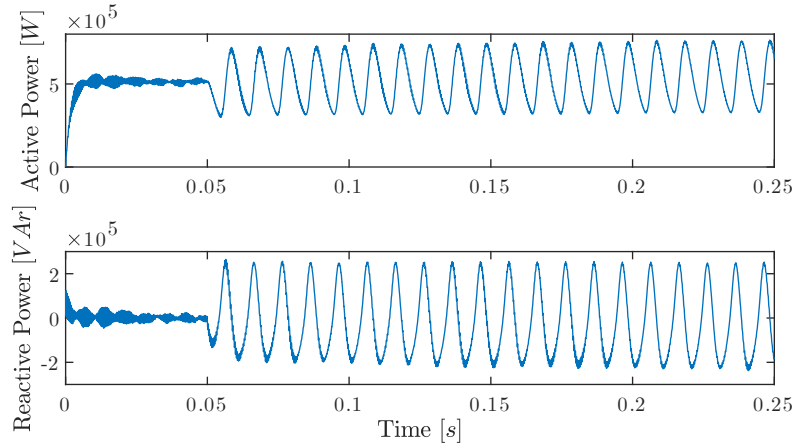


Figure 4.12: P and Q injection using the original PI controller with setpoint $P = 500$ kW, $Q = 0$ VAr, short at $t = 0.05$ s. P oscillates between 328 and 760 kW, Q oscillates between -238 and 253 kVAr.

4.4.2 Adjusted PI Controller

Line Fault at Zero Phase Voltage

Because the setpoint tracking of the original PI controller had shown dissatisfactory results, it was decided to test an adjusted controller that would perform better at stabilising the power oscillations in the same fault conditions as the previous test. Simulations were run with the proportional term multiplied by different values. A multiplication by a factor of 10 ($K_p = 0.75$, $K_i = 0.55$) provided improved results in setpoint tracking, as shown in Figure 4.14. However, this controller exhibits higher peak currents, illustrated by Figure 4.13.

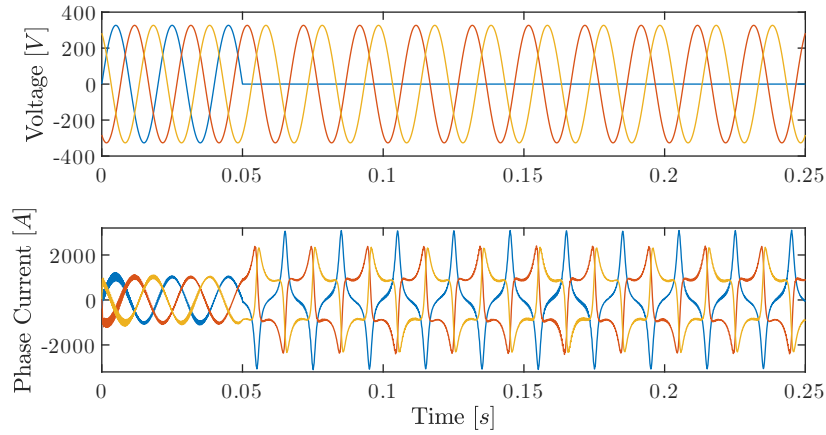


Figure 4.13: v_g and i_g using the adjusted PI controller, short at $t = 0.05$ s. Peak currents: $i_{ga} = 3.1$ kA, $i_{gb} = 2.4$ kA, $i_{gc} = 2.3$ kA.

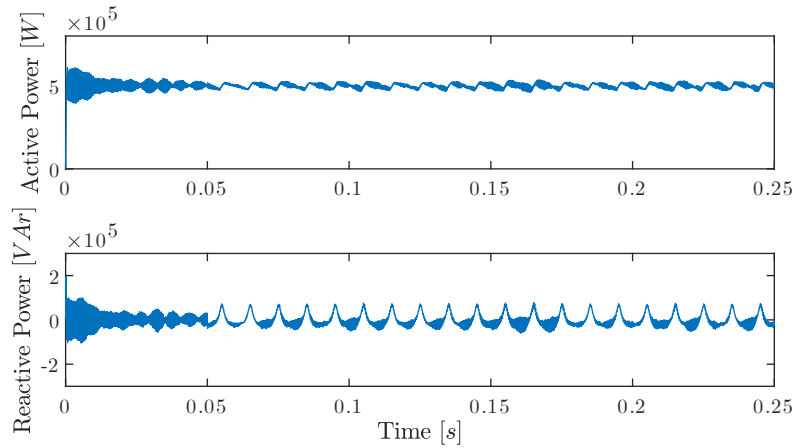


Figure 4.14: P and Q injection using the adjusted PI controller with setpoint $P = 500$ kW, $Q = 0$ VAr, short at $t = 0.05$ s. P oscillates between 465 and 521 kW, Q oscillates between -60 and 73 kVAr.

Line Fault at Phase Voltage Peak

Another test performed on the adjusted controller comprised the same line fault, but happening at the time when the phase voltage peaks 0.045 seconds after system start up. The initial current peak of 5 417 A was 1.77 times larger in comparison to the peak current of the previous test, but after a transient time of approx. 0.1 s the output of the system resembles the output of the previous test. This is shown by Figure 4.15. The current spike also affects the peak output power in Figure 4.16.

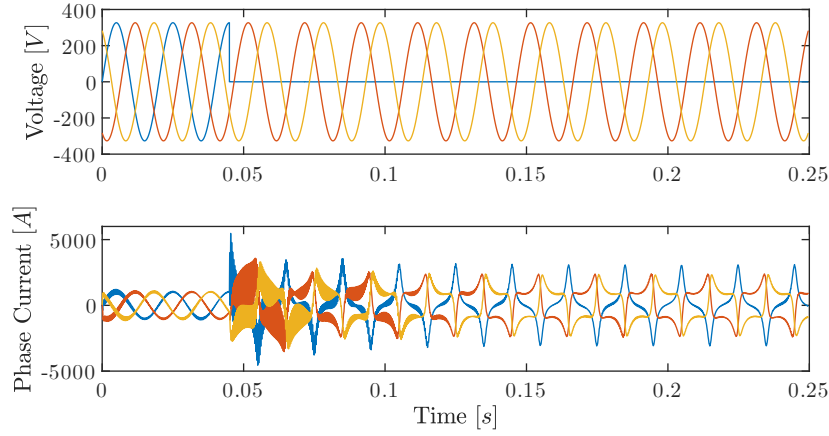


Figure 4.15: v_g and i_g using the adjusted PI controller, short at $t = 0.045$ s. Peak currents: $i_{ga} = 5.4$ kA, $i_{gb} = 3.6$ kA, $i_{gc} = 3.3$ kA.

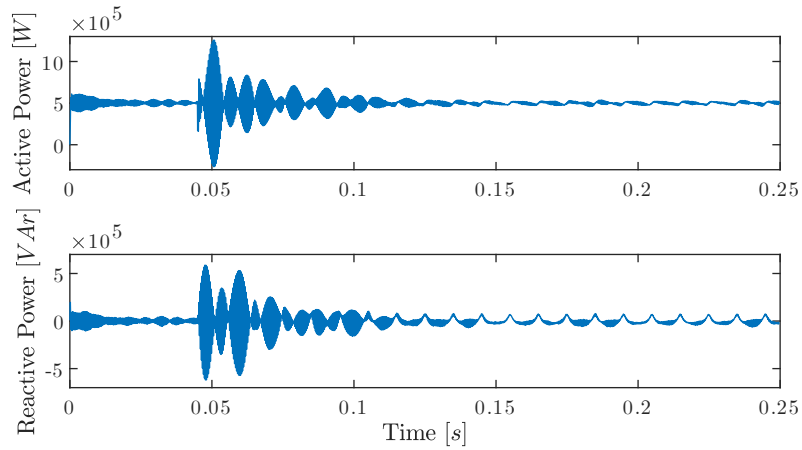


Figure 4.16: P and Q injection using the adjusted PI controller with setpoint $P = 500$ kW, $Q = 0$ VAr, short at $t = 0.045$ s. P peaks at 1.2 MW and oscillates between 465 and 521 kW, Q peaks at 588 kVAr and oscillates between -60 and 73 kVAr.

Response to Reconnection of the Grid at Phase Peak

This test was performed on the adjusted PI controller to validate the system against the DK1 grid standards, which requires that the system should be able to recover within 5 seconds as mentioned in Section 2.0.1. Similar to the previous tests of disconnection and short of the line, reconnection to the grid causes a transient response only if it happens during a non-zero phase voltage. Therefore, only the result of reconnecting the grid at 0.095 s, when the phase a voltage peaks, is shown in Figures 4.17 and 4.18. The transient time is around 0.1 s, which is within the requirements of the DK1 grid regulations.

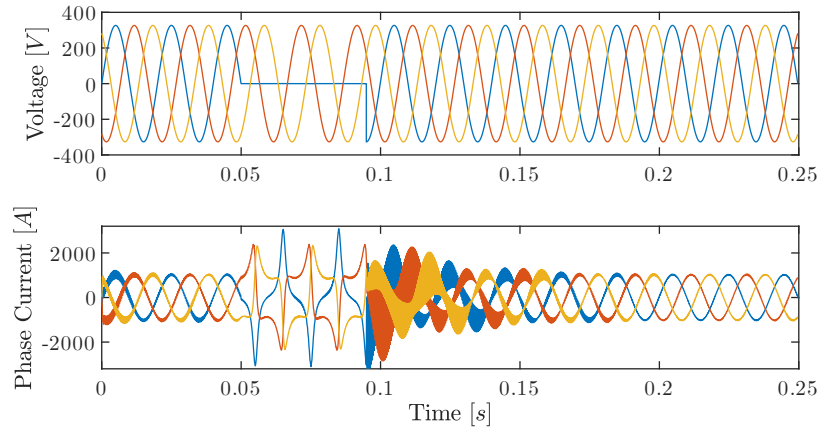


Figure 4.17: v_g and i_g using the adjusted PI controller, grid reconnection at $t = 0.095$ s.

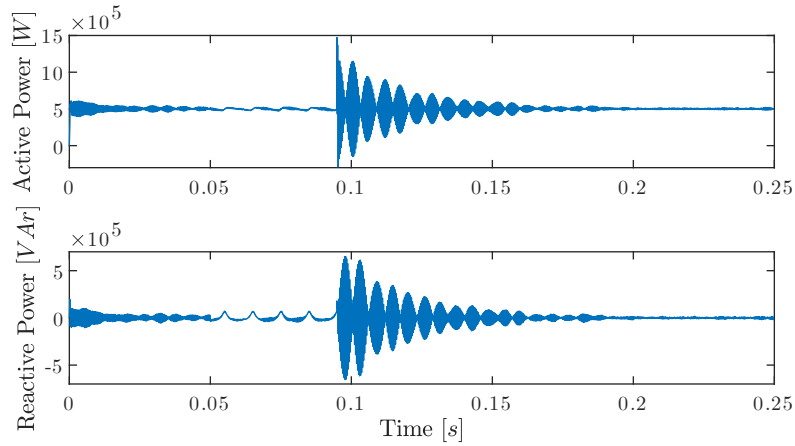


Figure 4.18: P and Q injection using the adjusted PI controller with setpoint $P = 500$ kW, $Q = 0$ VAr, and grid reconnection at $t = 0.095$ s. P peaks at 1.5 MW, Q peaks at 650 kVAr.

Chapter 5

Discussion and Conclusion

5.1 Discussion

During the course of the problem analysis phase, it was found that narrowing down a particular issue to solve proved to be more challenging than expected, as the specific application of battery power barges is a new implementation of technology where the main concerns are not yet clearly identified in the existing literature. Nevertheless, comparing control methods and inverter structures will definitely be among considerations that are necessary to make when such a system is to be designed.

With the goal of clearly observing the role of the capacitor in filtering, the inductances were calculated for the LCL filter and then by removing the capacitor, the total inductance was used for the L filter. If the inductance was calculated specifically for the L filter, it may have performed better with regard to harmonic distortion. Observing Table 4.3, the largest distortions for the L filter were found in the switching frequency range which was not the case for the LCL filter tests, which shows that the capacitor does filter out the higher frequencies. For the LCL tests it also showed that the control can greatly affect the harmonic placement. The state space controller showed the overall lowest THD and the largest harmonics around the lower end of the frequency spectrum, while the PI controller had the bulk of its distortion issues around the resonant frequency of the filter. However, further tuning of the controller and the notch filter could possibly improve this. Based on this, it is likely that LCL filters are preferable for grid-tied applications. However, this could change depending on the application and strength of the grid, and L filters may be acceptable in some instances. Overall, all the configurations met the THD requirements specified in Section 2.0.1.

Had the SS LCL configuration not had issues with reference tracking and transient response, it may have been the better option for control, due to the significantly lower THD.

An additional advantage of state-space control, aside from the low THD, is that state observers can be implemented, minimising the number of sensors required in the system. It could thus have an added benefit of cost efficiency, though at some cost of complexity of the control system compared to a PI controller.

With the PI LCL configuration, further tests were conducted to observe the performance under non-ideal conditions. Regarding the requirements to operate at different grid stiffness levels, it was found that the system starts to comply with the required distortion thresholds at a SCR between 160 and 185, and it failed to achieve suitable THD values for weaker grids. A case of line fault was also simulated, and the system managed to return to normal operation in 0.1 seconds for the worst-case scenario, when a line shorts or reconnects at its voltage peak, which complies with the requirements for DK1.

5.2 Conclusion

The main aim of the project was to compare two different control methods to see how well they perform with regards to the requirements for grid connection, as this is a consideration that will need to be made in the future for developing battery power barges. The choice of control method in this case favours PI control, as it could fulfil requirements of harmonic distortion as well as reference tracking, and further tuning could likely improve the results. This does not distinctly rule state-space control out, however, it could not be successfully tuned for all tests in this project.

The report additionally investigated and concluded that LCL filters are a fitting choice for grid-tied applications due the low harmonic distortion that can be achieved, as was particularly shown with the state-space control. The capacitor was thus shown to play an important role in filtering.

Future work on this project could include further tuning and robustness testing of the controller, and additional considerations of battery dynamics could be added. Ultimately, the goal of the investigation is to contribute to physical implementations within the battery powered barge area.

Bibliography

- [1] David Nickerson. *The History of Power Barges*. Accessed 03-03-2024. URL: <https://energycentral.com/c/iu/history-power-barges>.
- [2] EPCM Holdings. *A Case or Two or Three for Floating Power Plants*. Accessed 03-03-2024. URL: <https://epcmholdings.com/a-case-or-two-or-three-for-floating-power-plants>.
- [3] Arthur Neslen. “Wind power generates 140% of Denmark’s electricity demand”. In: *The Guardian* (2015). Accessed 03-03-2024. URL: <https://www.theguardian.com/environment/2015/jul/10/denmark-wind-windfarm-power-exceed-electricity-demand>.
- [4] U.S. Department of Commerce International Trade Administration. *Uruguay - Country Commercial Guide*. Accessed 03-03-2024. URL: <https://www.trade.gov/country-commercial-guides/uruguay-renewable-energy-equipment>.
- [5] Fundación Valenciaport. *Bluebarge – Blue Bunkering of Anchored Ships with Renewable Generated Electricity*. [Accessed 26-02-2024]. 2024. URL: <https://www.fundacion.valenciaport.com/en/project/bluebarge/>.
- [6] Zhuzhu Song et al. “Implications of government subsidies on shipping companies’ shore power usage strategies in port”. In: *Transportation Research Part E: Logistics and Transportation Review* 165 (2022), p. 1. ISSN: 1366-5545. DOI: <https://doi.org/10.1016/j.tre.2022.102840>. URL: <https://www.sciencedirect.com/science/article/pii/S1366554522002228>.
- [7] Transoceanic Group. *Power Barge Project*. Accessed 03-03-2024. URL: <https://transoceanic.group/power-barge.html>.
- [8] World Nuclear News. *Russia connects floating plant to grid*. [Accessed 06-03-2024]. 2019. URL: <https://www.world-nuclear-news.org/Articles/Russia-connects-floating-plant-to-grid>.

- [9] Fabrizio Sossan and Fernando Alvarado. "Battery Energy Storage Systems for Applications in Distribution Grids". In: *Planning and Operation of Active Distribution Networks: Technical, Social and Environmental Aspects*. Ed. by Antonio Carlos Zambroni de Souza and Bala Venkatesh. Cham: Springer International Publishing, 2022, pp. 153–180. ISBN: 978-3-030-90812-6. DOI: 10.1007/978-3-030-90812-6_6. URL: https://doi.org/10.1007/978-3-030-90812-6_6.
- [10] GloMEEP. *Shore-to-ship power converters*. Accessed 03-03-2024. URL: <https://glomeep.imo.org/technology/shore-power>.
- [11] Energinet. *TECHNICAL REGULATION 3.3.1 FOR ELECTRICAL ENERGY STORAGE FACILITIES*. [Accessed 28-02-2024]. 2019. URL: <https://en.energinet.dk/media/5rqbtv5w/technical-regulation-3-3-1-for-electrical-energy-storage-facilities.pdf>.
- [12] Dynapower. *CPS-i Battery Energy Storage System Datasheet*. Accessed 03-03-2024. URL: <https://dynapower.com/wp-content/uploads/2021/12/CPS-i-Datasheet.pdf>.
- [13] Saft. *Intensium Shift Energy Storage lineup Brochure*. Accessed 03-03-2024. URL: <https://www.saft.com/products-solutions/products/intensium-shift>.
- [14] Danfoss. *Race for fuel savings also boosts air quality at CCB Bergen*. Accessed 03-03-2024. 2016. URL: <https://www.danfoss.com/en/service-and-support/case-stories/dds/race-for-fuel-savings-also-boosts-air-quality-at-ccb-bergen/>.
- [15] ABB. *Shore-to-ship power converters*. Accessed 03-03-2024. 2024. URL: <https://new.abb.com/power-converters-inverters/grid-interconnections/shore-to-ship-converters>.
- [16] Danfoss. *Selection Guide Vacon NXP Grid Converter*. 2015. URL: https://files.danfoss.com/download/Drives/DKDDPB914A102_NXP_Grid_Converter.pdf.
- [17] Danfoss. *Vacon NX AC Drives ARFIF106 Grid Converter with General Grid Codes Application manual*. 2020. URL: <https://files.danfoss.com/download/Drives/Vacon-NXP-Grid-Converter-GGC-ARFIF106V122-Manual-DPD01978A-UK-V001.pdf>.
- [18] ABB. *PCS100 ESS Grid Connect Interface for Energy Storage Systems: User Manual*. 2021. URL: https://library.e.abb.com/public/8b613f6b51914388b996de018db1dd22/2UCD190000E001_j%20PCS100%20ESS%20User%20Manual.pdf.
- [19] Siemens. *Sinamics S120 Grid infeed. System Manual*. 2020. URL: <https://support.industry.siemens.com/cs/document/109476635/sinamics-s120-system-manual-grid-infeed?dti=0&lc=en-DK>.

- [20] Guishi Wang et al. "A Review of Power Electronics for Grid Connection of Utility-Scale Battery Energy Storage Systems". In: *IEEE Transactions on Sustainable Energy* 7 (2016), pp. 7,8. DOI: 10.1109/TSTE.2016.2586941. URL: https://www.researchgate.net/publication/305037268_A_Review_of_Power_Electronics_for_Grid_Connection_of_Utility-Scale_Battery_Energy_Storage_Systems.
- [21] Marco Stecca et al. "Comparison of Two and Three-Level DC-AC Converters for a 100 kW Battery Energy Storage System". In: *2020 IEEE 29th International Symposium on Industrial Electronics (ISIE)* (2020), p. 681. DOI: 10.1109/ISIE45063.2020.9152545. URL: <https://ieeexplore.ieee.org/document/9152545>.
- [22] Michael Schimpe et al. "Energy efficiency evaluation of grid connection scenarios for stationary battery energy storage systems". In: *Energy Procedia* 155 (Nov. 2018), pp. 81,84–95. DOI: 10.1016/j.egypro.2018.11.065.
- [23] Amirnaser Yazdani and Reza Iravani. *Voltage-Sourced Converters in Power Systems: Modeling, Control and Applications*. John Wiley & Sons, Inc, 2010.
- [24] Muhammad H. (Muhammad Harunur) Rashid, Narendra Kumar, and Ashish R. (Ashish Rajeshwar) Kulkarni. *Power electronics : devices, circuits and applications*. 4. ed., International edition. Harlow: Pearson, 2014, p. 341. ISBN: 9780273769088.
- [25] Chuan Xie et al. "Modeling and control of LCL-filtered grid-tied inverters with wide inductance variation". In: (2017), pp. 1293–1298. DOI: 10.1109/IECON.2017.8216220.
- [26] Marco Liserre, Frede Blaabjerg, and Antonio Dell'Aquila. "Step-by-step design procedure for a grid-connected three-phase PWM voltage source converter". eng. In: *International journal of electronics* 91.8 (2004), p. 446. ISSN: 0020-7217.
- [27] Anca Julean, Mihai Ciobotaru, and Lucian Asiminoaei. "Active Damping of LCL Filter Resonance in Grid Connected Applications". In: (2009). URL: <https://api.semanticscholar.org/CorpusID:33484218>.
- [28] Sabbir Hasan et al. "The LCL filter design for three phase DC-AC voltage converter The LCL filter design for three phase DC-AC voltage converter". In: *Journal of Physics: Conference Series* 1783 (Feb. 2021), p. 3. DOI: 10.1088/1742-6596/1783/1/012067.
- [29] M. Liserre, F. Blaabjerg, and S. Hansen. "Design and control of an LCL-filter-based three-phase active rectifier". In: *IEEE Transactions on Industry Applications* 41.5 (2005), pp. 1281–1291. DOI: 10.1109/TIA.2005.853373.
- [30] Emre Kantar, S.Nadir Usluer, and Ahmet Hava. "Design and performance analysis of a grid connected PWM-VSI system". In: (Nov. 2013), p. 159. DOI: 10.1109/ELEC0.2013.6713823.
- [31] Peng Zhan et al. "Design of LCL filters for the back-to-back converter in a Doubly Fed Induction Generator". In: (2012), p. 2. DOI: 10.1109/ISGT-Asia.2012.6303305.

- [32] Pekik Argo Dahono. "A control method to damp oscillation in the input LC filter". In: *2002 IEEE 33rd Annual IEEE Power Electronics Specialists Conference. Proceedings (Cat. No.02CH37289)* 4 (2002), 1630–1635 vol.4. URL: <https://api.semanticscholar.org/CorpusID:110484345>.
- [33] TDK Electronics AG. *EMC filters LCL filters 300/520 V, 50/60 Hz, 16 A ... 400 A, 50 °C Series/Type: B84143G*R/S405*. 2021. URL: https://www.tdk-electronics.tdk.com/inf/30/db/emc_2014/B84143G_405.pdf.
- [34] Chi Zhang et al. "Resonance damping techniques for grid-connected voltage source converters with LCL filters — A review". In: (2014), p. 1. DOI: 10.1109/ENERGYCON.2014.6850424.
- [35] Rafael Peña-Alzola et al. "Analysis of the Passive Damping Losses in LCL-Filter-Based Grid Converters". In: *IEEE Transactions on Power Electronics* 28.6 (2013), p. 1. DOI: 10.1109/TPEL.2012.2222931.
- [36] Ronald Jackson, Shamsul Aizam, and Suriana Salimin. "A Sequence Rules Analysis on Active and Passive LCL filter for Three-Phase Inverter-Grid Connection for Damping Stability Consideration". In: *International Journal of Renewable Energy Research* 10 (2020), p. 2.
- [37] Rafael Peña-Alzola et al. "LCL-Filter Design for Robust Active Damping in Grid-Connected Converters". In: *IEEE Transactions on Industrial Informatics* 10 (Nov. 2014), p. 1. DOI: 10.1109/TII.2014.2361604.
- [38] A.A. Rockhill et al. "Grid Filter Design for a Multi-Megawatt Medium-Voltage Voltage Source Inverter". English. In: *IEEE Transactions on Industrial Electronics* 58.4 (2011), p. 1208. ISSN: 0278-0046. DOI: 10.1109/TIE.2010.2087293.
- [39] Mehmet Büyük et al. "Topologies, generalized designs, passive and active damping methods of switching ripple filters for voltage source inverter: A comprehensive review". In: *Renewable and Sustainable Energy Reviews* 62 (2016), p. 53. ISSN: 1364-0321. DOI: <https://doi.org/10.1016/j.rser.2016.04.006>. URL: <https://www.sciencedirect.com/science/article/pii/S1364032116300235>.
- [40] Camilo C. Gomes, Allan F. Cupertino, and Heverton A. Pereira. "Damping techniques for grid-connected voltage source converters based on LCL filter: An overview". In: *Renewable and Sustainable Energy Reviews* 81 (2018), p. 18. ISSN: 1364-0321. DOI: <https://doi.org/10.1016/j.rser.2017.07.050>. URL: <https://www.sciencedirect.com/science/article/pii/S1364032117311206>.
- [41] Mehrdad; Hojabri Mojan; Hojabri and Arash Toudeshki. "Passive Damping Filter Design and Application for Three-Phase PV Grid-Connected Inverter". In: *International Journal of Electrical, Electronics and Data Communication (IJEEDC)* 3 (2015), pp. 17–18.

- [42] Dawn Tilbury and Bill and Messner. *Inverted Pendulum: State-Space Methods for Controller Design*. 2022. URL: <https://ctms.engin.umich.edu/CTMS/index.php?example=InvertedPendulum§ion=ControlStateSpace#6> (visited on 04/24/2024).
- [43] Gene F. Frankling, J. David Powell, and Abbas Emami-Naeini. *Feedback Control of Dynamic Systems, Eighth Edition*. Pearson Education Limited, 2020.
- [44] Ning Gai et al. *Active Disturbance Rejection Control Based on Extended State Observer for Three-Phase Battery Energy Storage Power Conversion System with LCL Filter*. 2022. DOI: 10.1007/s42835-021-00974-4.
- [45] The MathWorks Inc. *Varying Notch Filter*. URL: <https://se.mathworks.com/help/control/ref/varyingnotchfilter.html> (visited on 04/29/2024).
- [46] Aswad Adib et al. "On Stability of Voltage Source Inverters in Weak Grids". In: *IEEE Access* 6 (2018), pp. 4427–4439. DOI: 10.1109/ACCESS.2017.2788818.
- [47] Hendrik Just. *Modeling and control of power converters in weak and unbalanced electric grids*. Elektrische Energietechnik an der TU Berlin ; Band 12. Universitätsverlag der TU Berlin, 2021, pp. 15–16. ISBN: 3-7983-3207-X.
- [48] B. Blazic and I. Papic. "Voltage profile support in distribution networks - influence of the network R/X ratio". In: *2008 13th International Power Electronics and Motion Control Conference* (2008), p. 1.

Appendix A

Matlab Modelling Code

A.1 Matlab Code for PI L/LCL Control Derivation

```
1  %Define filter values
2  C_f = 497e-6;
3  L_inv = 1.4338e-04;
4  L_grid = 6.6909e-06;
5  R_inv = 0.7e-3;
6  R_grid = 0.4e-3;
7  R_tot = R_inv+R_grid;
8  L_tot = L_inv + L_grid;
9  tau = 2e-3;
10
11 %Calculate PI controller
12 k_p = (L_tot)/tau;
13 k_i = R_tot/tau;
14 cont = pid(k_p, k_i);
15
16 %LCL TF with parasitic resistances
17 LCL_tf = 1/( (C_f*L_grid*L_inv*s^3) + ...
18             ( ((L_grid*R_inv) + (L_inv*R_grid))*s^2) + ...
19             ((L_tot + (C_f*R_inv*R_grid))*s) + ...
20             R_inv + R_grid)
21
22 %L TF with parasitic resistance
23 L_tf = 1/(L_tot*s + R_tot)
24
```

```

25 sys_cl_LCL = feedback(LCL_tf*cont,1);
26 sys_cl_L = feedback(L_tf*cont,1);
27
28 %Check system response and characteristics
29 %damp(syscl)
30 step(sys_cl_LCL, sys_cl_L);

```

A.2 Matlab Code for L State Space Control Derivation

```

1  %Define filter values
2  L_inv = 1.4338e-04;
3  L_grid = 6.6909e-06;
4  L_tot = L_inv+L_grid;
5  C_f = 497e-06;
6  R_inv = 0.7e-3;
7  R_grid = 0.4e-3;
8  R_tot = R_inv+R_grid;
9  w = 50*2*pi;
10
11 % Define matrices
12 A = [w -R_tot/L_tot;
13      -R_tot/L_tot -w];
14 B = [1/L_tot 0;
15      0 1/L_tot];
16 C = [1 0; 0 1];
17 D = [0 0 ; 0 0];
18
19 sys = ss(A,B,C,D);
20
21 %%Calculate feedback using LQR
22 Q = [100 0;
23      0 100];
24 R=1;
25 [K,S,E]=lqr(A,B,Q,R)
26
27 %Reference input gain
28 N=[A B; C D]^-1*[0;0;0;1];
29 Nr=N(4)+K*N(2:3);
30 Nr = [Nr(1,1) ; Nr(1,1)]

```



```

31
32 %Define system with feedback gain K and reference gain Nbar
33 Ac=A-B*K;
34 Bc=B*Nr;
35 Cc=C;
36 Dc= [0];
37 syscl=ss(Ac,Bc,Cc,Dc);
38
39 %Check system response and characteristics
40 step(syscl);
41 damp(syscl);

```

A.3 Matlab Code for LCL State Space Control Derivation

```

1 %Define filter values
2 L_inv = 1.4338e-04;
3 L_grid = 6.6909e-06;
4 C_f = 497e-06;
5 R_inv = 0.7e-3;
6 R_grid = 0.4e-3;
7
8 % Vectors X and U(For reference).
9 %X = [I1D I2D Vcfd];
10 %U = [v_inv_D];
11
12 % Define matrices
13 A = [-R_inv/L_inv 0 -1/L_inv;
14      0 -R_grid/L_grid 1/L_grid;
15      1/C_f -1/C_f 0];
16 B = [1/L_inv; 0; 0];
17 C = [0 1 0];
18 D = [0];
19
20 %Calculate feedback using LQR
21 Q = [1 0 0;
22      0 100 0;
23      0 0 1];
24 R = 1;
25 K = lqr(A,B,Q,R)

```

```

26
27 %Calculate reference gain Nbar
28 N=[A B; C D]^-1*[0;0;0;1];
29 Nr=N(4)+K*N(1:3)
30
31 %Define system with feedback gain K and reference gain Nbar
32 Ac=A-B*K;
33 Bc=B*Nr;
34 Cc=C;
35 Dc=D;
36 syscl=ss(Ac,Bc,Cc,Dc);
37
38 %Check system response and characteristics
39 damp(syscl)
40 step(syscl);

```

A.4 Matlab Code for Calculating L_{grid} and R_{grid} for Weak Grids

```

1 E_n = 400;          % (V)    Grid Line to Line Voltage
2 S_n = 500000;       % (kVA)  Output Power of the Inverter
3 f = 50;             % (Hz)   Frequency of grid volta
4
5 % Use arrays to define the SCR values and initialize R_grid and L_grid
6 SCR_values = [93, 105, 139, 160, 185];
7 R_grid = zeros(size(SCR_values));
8 L_grid = zeros(size(SCR_values));
9
10 % Calculate R_grid and L_grid for each SCR value
11 for i = 1:length(SCR_values)
12     R_grid(i) = ((E_n)^2)/(SCR_values(i)*S_n*sqrt(1+(pi*f)^2));
13     L_grid(i) = R_grid(i) / 2;
14 end
15
16 % Display results
17 fprintf('%-12s %-20s %-20s\n', 'SCR Values', 'R_grid Values', 'L_grid Values');
18 for i = 1:length(SCR_values)
19     fprintf('%-12d %-20.10e %-20.10e\n', SCR_values(i), R_grid(i), L_grid(i));
20 end

```

Appendix B

Simulink Figures

Printscreens of the system split into subsystems for better readability.

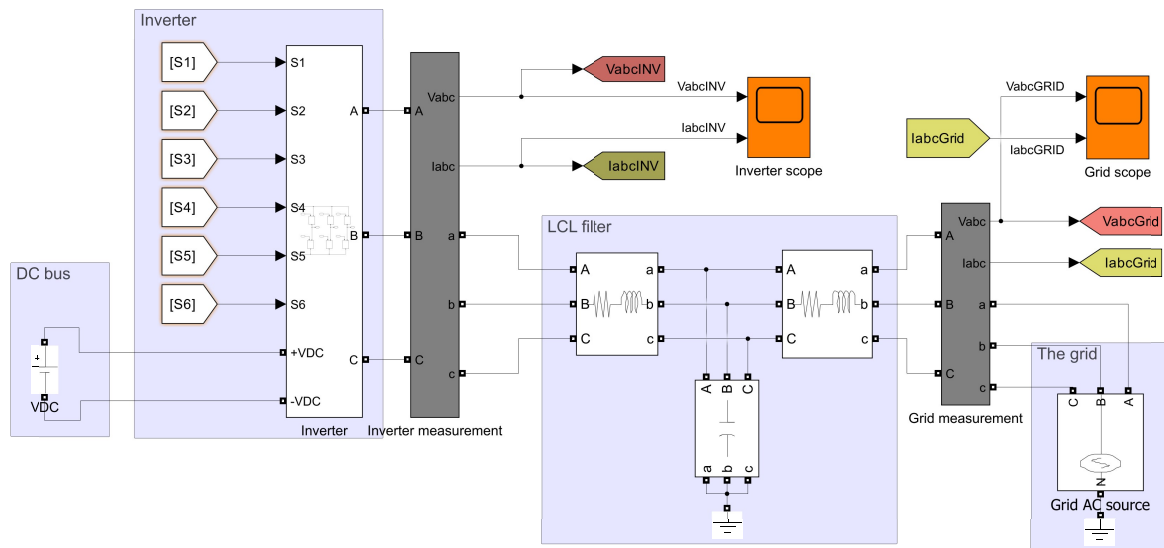


Figure B.1: Main blocks of the system.

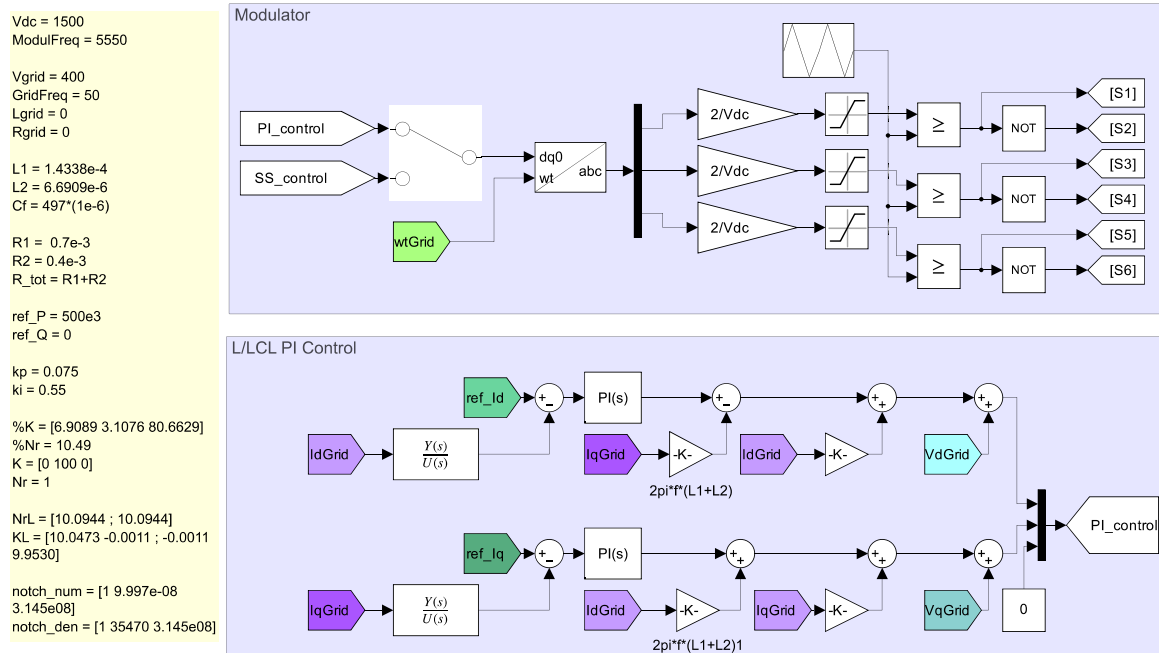


Figure B.2: Simulation variables and the modulator and PI controller.

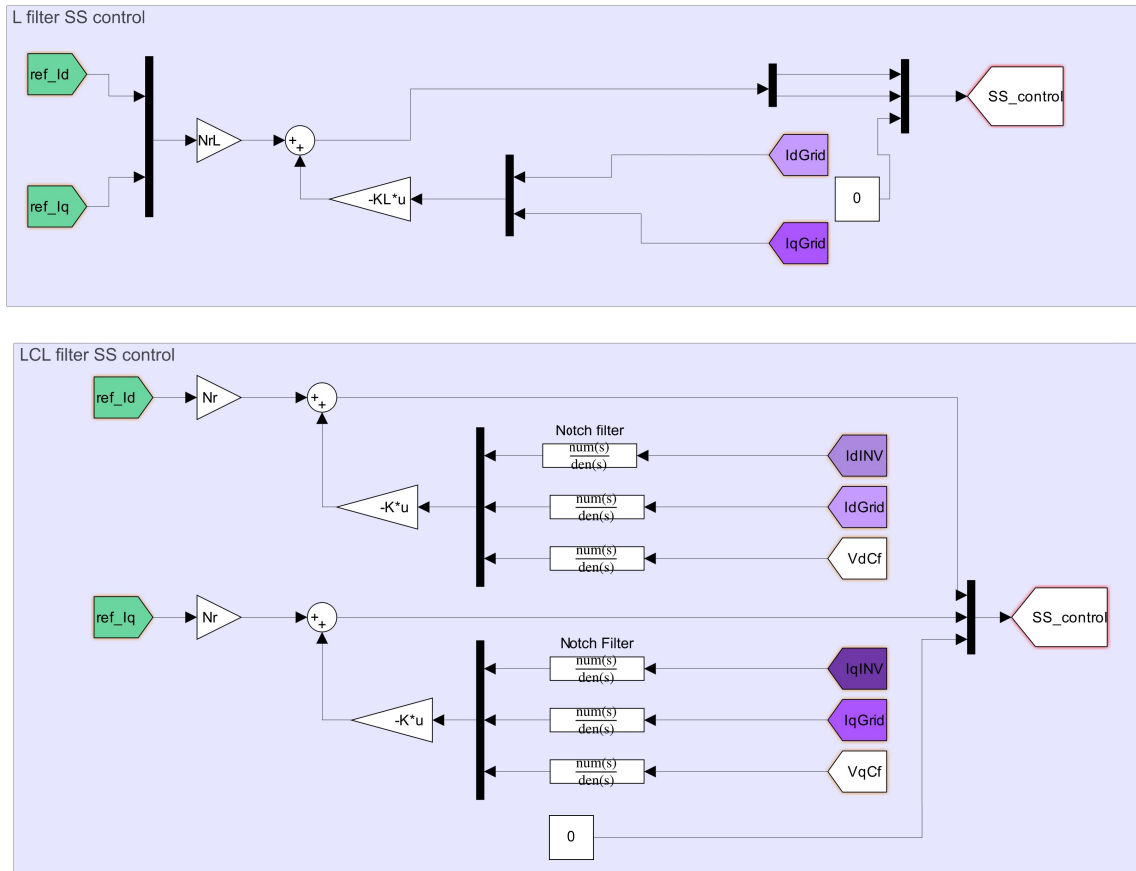


Figure B.3: State-space controllers.

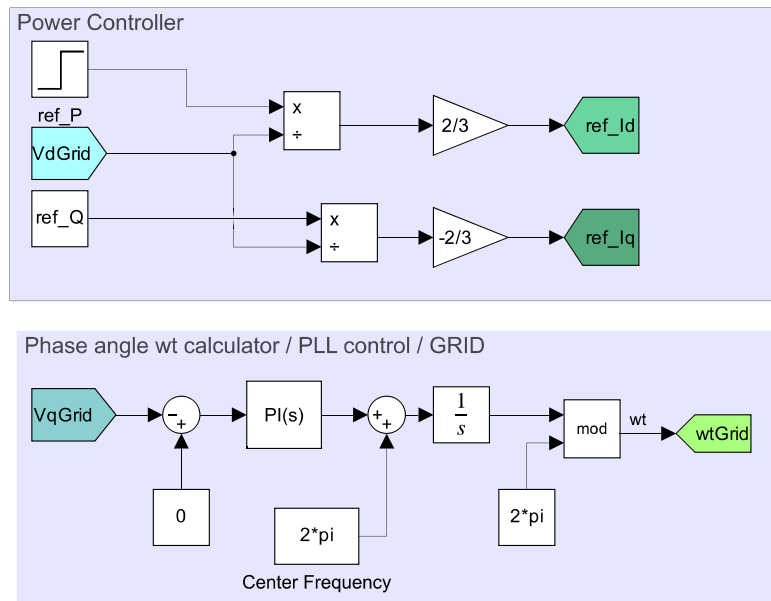


Figure B.4: Power controller and PLL blocks.